The Impact of the Amazon on the Biological Pump and the Air-Sea CO2 Balance of the Western Tropical Atlantic

Author(s):
Louchard, Domitille; Gruber, Nicolas; Münnich, Matthias

Publication date:
2021-06

Permanent link:
https://doi.org/10.3929/ethz-b-000492845

Originally published in:
Global Biogeochemical Cycles 35(6), https://doi.org/10.1029/2020GB006818

Global Biogeochemical Cycles

RESEARCH ARTICLE
10.1029/2020GB006818

The Impact of the Amazon on the Biological Pump and the Air-Sea CO_2 Balance of the Western Tropical Atlantic

Domitille Louchard[1], Nicolas Gruber[1], and Matthias Münnich[1]

[1]Environmental Physics, Institute of Biogeochemistry and Pollutant Dynamics, ETH Zurich, Zürich, Switzerland

Key Points:

- The Amazon River stimulates the biological pump in the WTA beyond a strict utilization of the riverine nutrients
- Diatom-diazotrophic assemblages, benefiting from the river supplied phosphorus, provide the required extra nitrogen
- The Amazon-driven stimulation of the biological pump induces a strong uptake of CO_2 from the atmosphere

Supporting Information:

Supporting Information may be found in the online version of this article.

Correspondence to:

D. Louchard,
domitille.louchard@usys.ethz.ch

Citation:

Louchard, D., Gruber, N., & Münnich, M. (2021). The impact of the Amazon on the biological pump and the air-sea CO_2 balance of the Western Tropical Atlantic. *Global Biogeochemical Cycles*, *35*, e2020GB006818. https://doi.org/10.1029/2020GB006818

Received 2 SEP 2020
Accepted 4 MAY 2021

Abstract The Amazon River strongly modifies the biogeochemistry of the Western Tropical Atlantic (WTA). To disentangle the different mechanisms driving these modifications, we conduct a series of modeling experiments with a high-resolution regional ocean model (ROMS) coupled to a biogeochemical/ecological model (BEC) that we augmented to include Diatom-Diazotroph-Assemblages (DDAs). In our model, the Amazon River increases net primary production (NPP) in the WTA by almost 10%, exceeding the stimulation expected from the supplied inorganic nitrogen and phosphorus by a factor of two. This amplification is fueled by new nitrogen stemming from DDA-driven N_2 fixation in the plume region, supported, in part, by the consumption of riverine dissolved organic phosphorus. The vertical export of organic carbon is enhanced by a shift of the phytoplankton community toward diatoms induced by the large amount of $Si(OH)_4$ delivered by the Amazon. These changes in NPP and export production induce a strong uptake of atmospheric CO_2. In contrast, the remineralization of the river-delivered terrestrial organic matter leads to a release of CO_2 over the WTA, which is partially offset by a net uptake induced by the riverine dissolved inorganic carbon and alkalinity. Overall, the Amazon reduces the strong outgassing of the WTA in our simulations by more than 50%. Our study demonstrates how rivers modify the marine biological pump and the air-sea CO_2 fluxes in the downstream ocean through a myriad of cascading effects, highlighting the need to fully consider the land-ocean aquatic continuum in the modeling of the Earth System.

1. Introduction

From its upland basin to the open ocean, the Amazon River connects the world's most productive rainforest to the oligotrophic Western Tropical Atlantic (WTA), that is, the region bounded by the equator in the south, 24°N in the north, the Lesser Antilles in the west, and 30°W in the east. Every second, the Amazon delivers about 190,000 m^3 of turbid freshwater rich in nutrients and organic matter, altering both the physical and biogeochemical properties of the ocean over up to 1.6 millions of km^2, that is, more than 15% of the WTA (Araujo et al., 2017; Coles et al., 2013; Gouveia et al., 2019; Ward et al., 2017).

Once most of the sediment load has settled and the water cleared up, the massive discharge of riverine nutrients spawns a large and persistent phytoplankton bloom (Da Cunha & Buitenhuis, 2013; Dagg et al., 2004; Smith & Demaster, 1996). Many dedicated in situ sampling programs have demonstrated that this high productivity is sustained by coastal diatoms and predominantly located on the continental shelf and along the northward pathway of the plume (Araujo et al., 2017; Demaster & Pope, 1996; Gouveia et al., 2019; Smith & Demaster, 1996). As the riverine nutrients are being drawn down by marine phytoplankton, the high ratio of $Si(OH)_4$ to NO_3 within the Amazon waters causes $Si(OH)_4$ in the plume waters further offshore to remain elevated when NO_3 becomes exhausted (Goes et al., 2014; Subramaniam et al., 2008; Weber et al., 2017). This effect is exacerbated by the dynamics at the sediment interface: The Amazon plume initially follows the coast northward on the North Brazilian shelf, where benthic denitrification creates an additional sink for NO_3 (Aller et al., 1996). The resulting deficiency of NO_3 relative to PO_4 and $Si(OH)_4$ is thought to provide the conditions that foster high rates of N_2 fixation supported primarily by Diatom-Diazotroph-Assemblages (DDAs) (Foster & Capone, 2012; Foster & O'Mullan, 2008; Subramaniam et al., 2008). DDAs are symbioses between diatoms of various genera (mostly *Hemiaulus* and *Rhizosolenia* in the WTA) and a diazotrophic cyanobacteria (*Richelia intracellularis*). The symbiont reduces nitrogen and provides ammonia to its host, while the host provides shelter and improves access to the limiting nutrients (Foster et al., 2011). As this symbiosis involves a large siliceous diatom, DDAs may be much more efficient in exporting the fixed organic carbon to depth compared to other more common diazotrophs such as *Trichodesmium*. Thus, DDAs

have been hypothesized to be the main pathway of carbon export within the plume waters (Subramaniam et al., 2008; Yeung et al., 2012). Furthermore, the newly introduced fixed nitrogen can fuel more biological production downstream in the very oligotrophic WTA, where NO_3 levels are almost always below detection (Hansell & Follows, 2008).

The enhancement of the marine biological pump by the Amazon River is recognized as a crucial factor for the CO_2 undersaturation typical of the plume waters driving an uptake of CO_2 from the atmosphere (Araujo et al., 2017; Subramaniam et al., 2008; Yeung et al., 2012). Estimates of this plume-related carbon sink range from 5 Tg C yr^{-1} (Lefévre et al., 2010) to 15 Tg C yr^{-1} (Cooley et al., 2007), reversing the expected paradigm of CO_2 release of the tropical ocean. But the impact of the Amazon on the air-sea CO_2 fluxes is more complex than just an enhancement of the biological pump. From the low-salinity waters, where terrestrial organic carbon is fueling heterotrophy (Lefèvre et al., 2017) and thus CO_2 out-gassing, to the open ocean, where the riverine input of Dissolved Inorganic Carbon (DIC) and Alkalinity (Alk) is diluted but still detectable (Cooley et al., 2007; Lefévre et al., 1998), the Amazon has a wide range of impacts that vary in space and time. Modeling experiments can help to disentangle the different contributions of the Amazon River to the air-sea CO_2 balance.

Only two studies have so far quantified the impact of the Amazon River on productivity and the air-sea CO_2 fluxes in the WTA. Da Cunha and Buitenhuis (2013) found a 5% increase in NPP and export production across the WTA, but the Amazon induced in their model only a modest reduction in the outgassing prevalent in the WTA. More recently, Lacroix et al. (2020) simulated an even larger relative enhancement of NPP, but they found the opposite effect on the air-sea CO_2 fluxes, that is, that the Amazon makes the outgassing of the WTA even stronger. They argued that this is primarily a consequence of the large input of terrestrial organic carbon, whose remineralization within the WTA produces an excess of CO_2 that drives outgassing. Both studies used global models with resolutions of the order of 100 km or more, raising questions about the fidelity of their modeling the complex circulation of the WTA. In particular, their model resolutions were too coarse to resolve mesoscale dynamics, which have been shown to play a crucial role in the dispersal of the plume (Coles et al., 2013; Fontes et al., 2008; Gouveia et al., 2019). In addition, neither study looked at the relative ratios of the different river-delivered organic and inorganic nutrients and in what way their interaction can shift for example, the phytoplankton community with potential consequences for export production. Most importantly, these studies did not include DDAs and thus potentially missed an important source of extra nitrogen that can fuel further ocean productivity downstream. DDAs were so far only accounted in the modeling study by Stukel et al. (2014). But they limited their focus on the factors controlling the blooms of DDAs, and thus did not investigate the impacts of the Amazon on the DDAs' export production or on the air-sea CO_2 exchange.

In this study, using a modeling approach, we aim to capture and quantify most of the physical and biogeochemical/ecological complexities associated with the impact of the Amazon on the biological pump and the air-sea CO_2 fluxes in the WTA. To this end, we use an eddy-resolving configuration of the Regional Oceanic Modeling System (ROMS) (Shchepetkin & McWilliams, 2005) coupled to a biogeochemical/ecological module (BEC) (Moore et al., 2013) that has been modified to include DDAs. We first investigate the response of NPP and carbon export based on different factorial simulations, where one or all the nutrients are removed from the Amazon River inflow (Section 3). We then quantify the overall effect of the Amazon River on the air-sea CO_2 balance from the mouth of the river to the open ocean and assess the contribution of the different processes controlling this balance (Section 4) paying special attention to the interaction of the different biogeochemical cycles and the cascading effects within these, that is, the fact that the outcome of one process induces changes in another process further downstream.

2. Materials and Methods

2.1. ROMS-BEC With Explicit DDAs

We use the UCLA-ETH version of the Regional Ocean Modeling system (ROMS, Shchepetkin and McWilliams [2005]), in which we updated the advection scheme for all tracers to the Weighted Essentially Non Oscillatory (WENO) scheme (Shu, 1998; Vandemeulebrouck, 2020), as this ensures higher accuracy while maintaining positivity. The model runs on a newly configured grid (576 × 450 grid points) that spans the

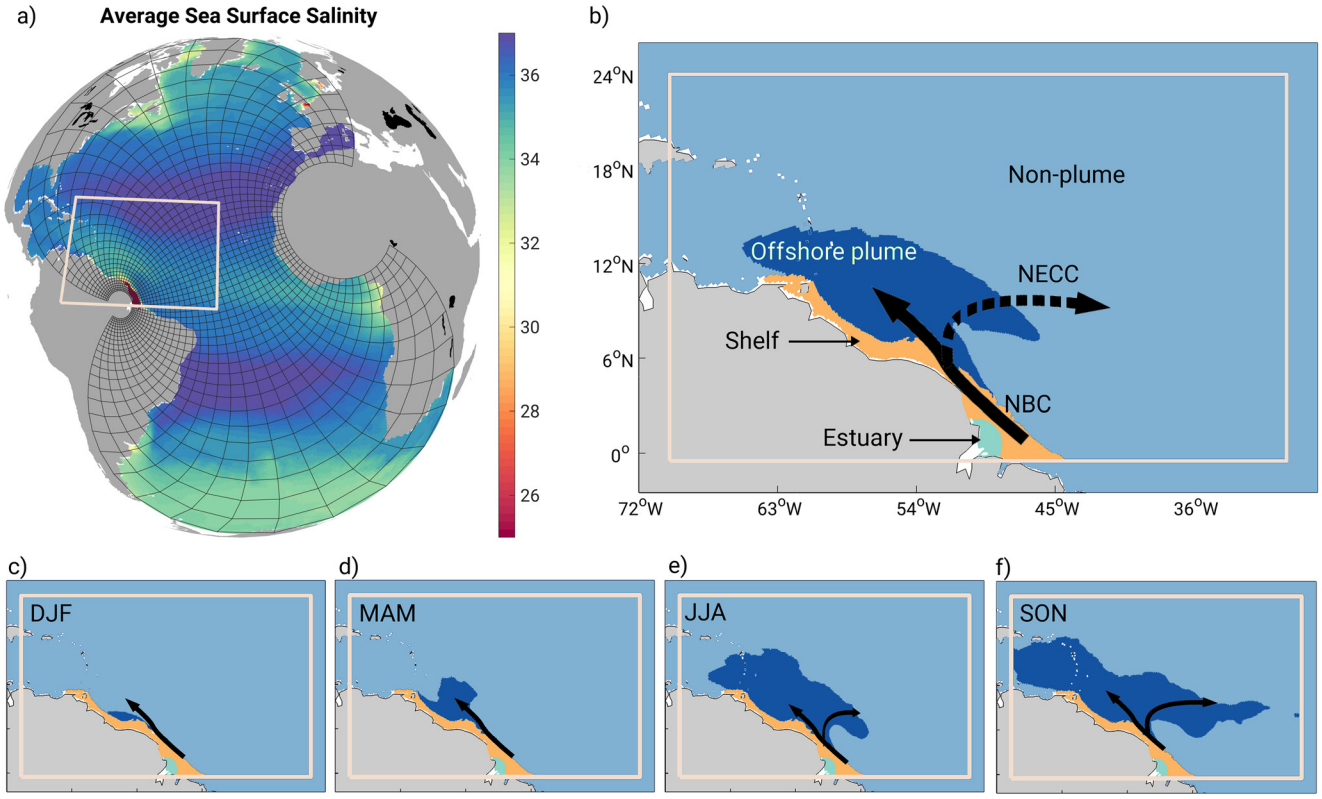

Figure 1. Maps of the model domain and the analysis regions: (a) Model domain showing the modeled annual average sea surface salinity, and the telescopic grid at by every 12th grid line. The white quadrilateral indicates our region of study (0.5°S–24°N; 30°–70°W) (b) Map of the analysis region with the annual average offshore plume and nonplume areas colored in dark and light blue, respectively. Black arrows indicate the North Brazilian Current (NBC) and the seasonally varying North Equatorial Counter Current (NECC). (c–f) Seasonal maps illustrating the evolution of the offshore plume and nonplume waters. See text for how we delineated the different areas.

whole Atlantic basin around two poles: one centered on the Amazon River mouth (0°N; 53°W) and the other one over Western Africa (18°N; 4°W) (Figure 1). This telescopic framework results in a high resolution in the tropical regions, from ~4 to ~14 km and a coarser resolution in the outskirts of the grid (from ~50 to ~120 km). In the vertical, the model is discretized with 42 sigma layers, with an enhanced resolution in the top 100 m. As a result, 18 layers are usually found within this depth range. The northern boundary toward the Arctic and the eastern boundary within the Mediterranean are closed, while the southern boundary toward the Southern Ocean is open.

ROMS is coupled to an ecological/biogeochemical model (BEC, Moore et al. [2013]) that resolves the cycling of carbon, oxygen and different macro and micro nutrients, namely nitrogen, phosphorus, silicon, and iron. These elements, along with light and temperature, govern the growth of four phytoplankton functional types (PFTs). The standard version of BEC includes diatoms, a generic small phytoplankton class, diazotrophs (representing the most abundant marine diazotroph, *Trichodesmium* spp.) and one zooplankton class. A fraction of the small phytoplankton PFT is modeled to consist of coccolithophores, with their associated formation of calcite.

We added to this model an explicit representation of DDAs. We allowed two states for the DDAs, that is, symbiotic and nonsymbiotic, depending on the seawater NO_3 concentration. DDAs are assumed to be in a nonsymbiotic state, that is, without a diazotrophic symbiont, when NO_3 is above 0.5 mmol N m^{-3}. In this case, we regard the DDAs as regular diatoms with the same half saturation constants for NO_3 and ammonium as the normal diatom class. This threshold was determined by analyzing in the database from Luo et al. (2012) the environmental NO_3 concentration present when the biomass of DDAs drops to near zero (Figure S1). Below our threshold, DDAs are truly represented as a symbiosis and are modeled by combining key traits of both diatoms and diazotrophs (Table S1). As diazotrophs, DDAs can fix N_2 for their nitrogen

needs, but require higher levels of iron to do so. In addition, DDAs, like *Trichodesmium*, can uptake dissolved organic phosphorus (DOP) with the same efficiency as they can take up PO_4, in agreement with several experimental studies (Girault et al., 2013; Watkins-Brandt et al., 2011). As diatoms, the growth of the DDAs is limited by $Si(OH)_4$. Upon death or grazing, their contribution to the pool of particulate organic carbon (POC) is the same as that of the regular diatoms (Table S1).

The C:N:P ratios of phytoplankton are fixed in BEC, with a stoichiometry close to the Redfield ratios: 117:16:1 for small phytoplankton, diatoms and DDAs (Anderson & Sarmiento, 1994), 117:45:1 for *Trichodesmium* (Letelier & Karl, 1998). The uptake and release of these macronutrients by phytoplankton follows the same ratios. If zooplankton is grazing on *Trichodesmium*, the phosphorus in excess compared to the standard Redfield ratio is assumed to be excreted immediately and split between the PO_4 pool (85%) and the DOP pool (15%). The ratios of Si:C, Fe:C, and Chl:C are not fixed and can vary depending on the ambient nutrient levels. Thus, the Si:C ratio of diatoms and DDAs increases when iron is depleted leading to a stronger silification. Conversely, it decreases when $Si(OH)_4$ is scarce (less than 2 mmol m^{-3}).

In BEC, POC is directly produced by phytoplankton through nongrazing mortality and aggregation. The single zooplankton class grazing on all PFTs also produces POC as a result of sloppy feeding, egestion and mortality. The vertical sinking flux of POC and its remineralization is modeled following the ballast/protection model of Armstrong et al. (2001), which assumes that sinking material is either free or associated with ballasting minerals. Ballasting minerals in ROMS-BEC include calcite from coccolithophores, silica from diatoms and DDAs, and mineral dust from atmospheric deposition. The composition of the particulate matter determines its remineralization/dissolution length scale, from which the organic matter remineralization rates are determined given the implicit sinking scheme of BEC. A fraction of POC and other particulate organic matter arriving at the sediments is buried following Dunne et al. (2007) with a fixed maximum of 80%. Sediment denitrification represents an additional loss term for nitrogen. The remaining fraction of particulate organic matter is immediately remineralized based on the early diagenesis model of Soetaert et al. (1996), feeding back the inorganic carbon and nutrient pools.

Around 15% of the produced organic matter in the euphotic zone is simulated to be channeled to the dissolved organic matter (DOM) pool. Due to the decoupling between production and remineralization of its C, N, and P fractions, DOM in BEC has a variable C:N:P stoichiometry. Upon production, a fraction of DOM is considered semi-labile, another refractory. Each DOM tracer has an assigned lifetime that varies depending on the light field in the considered grid cell. More specifically, it is assumed that the lifetime of DOM is shorter when the photosynthetically active radiation (PAR) is above 1% of surface irradiance and longer when PAR is below 1% (Table S2). Our parameterization and parameter values lead to a typical lifetime for semi-labile DOM ranging from 5 months (PAR > 1%) to 10 years (PAR < 1%), and for the refractory pool of DOM from 2.5 to 670 years, respectively.

2.2. External Sources of Nutrients

In the model, the Amazon River is represented as a three-dimensional influx boundary condition, supplying brackish water and dissolved constituents to the ocean (see Table S3). We placed the boundary within the Amazon estuary, so that the inflowing waters reflect already some mixture of pure Amazon waters and marine conditions, resulting in an annual mean salinity of 3.8. We prescribe monthly variations of discharge at this boundary, including its temperature and salinity as well as the dissolved constituents: alkalinity, dissolved inorganic/organic nutrients and dissolved organic/inorganic carbon (Table S3). We split the DIN estimate between NO_3 and NH_4 based on the NO_3:NH_4 ratio reported by Demaster and Aller (2001). The input concentration of all other state variables is set to zero. We obtained most of these input concentrations from a climatology that was derived from a comprehensive compilation of observations and model-based estimates (Araujo et al., 2014). We obtain the riverine input of dissolved organic nitrogen (DON) and DOP, by multiplying the input of DOC with a fixed stoichiometric ratio derived from the canonical C:N:P ratio of 117:16:1. Under this assumption, DON and DOP represent a significant component of the overall N and P inputs. Such a high organic nutrient contribution is typical for natural tropical river systems such as the Amazon (Seitzinger et al., 2005). We note that in light of the importance of DOP in our system, this assumption is nevertheless critical, which we will discuss in more detail in the caveat section. This contrasts with the stoichiometry of the inorganic nutrients (Table S3): In the annual mean, the N:P:Si ratios of the inputs

amount to 14:1:155, that is, the Amazon input is characterized by a slight excess of P over N (relative to the canonical Redfield ratio), and a very large excess of Si over both N and P (iron replete diatoms tend to draw down the nutrients with a N:P:Si ratio of about 1:16:1 (Brzezinski et al., 2003). In the model, all dissolved constituents are added to their corresponding marine semi-labile corresponding state variables, that is, once in the ocean, we do not differentiate between the terrestrial and marine sources of these constituents.

We do not consider the riverine input of any particulate matter in our model. The vast majority of the river supplied particulate matter sinks rapidly to the seafloor once the flow speed slows down upon arrival of the waters near the mouth of the river. At the seafloor, part of the material is buried, and part is remineralized, impacting the biogeochemistry of the water column indirectly. Although we do not explicitly model this process, we partly account for these remineralization fluxes through our parameterizations of the fluxes across the sediment-water interface.

In the estuary and near the mouth of the Amazon, where salinity is less than 31, we apply an attenuation coefficient to the PAR to account for the effects of river supplied colored dissolved organic matter (C-DOM) and turbidity on the vertical penetration of light. The attenuation coefficient is assumed to vary linearly with salinity, using a regression determined from in situ measurements by Del Vecchio and Subramaniam (2004), that is, $PAR_c = PAR \cdot (0.232 + S)$, where PAR_c is the PAR corrected for the additional attenuation, and S the local salinity (in practical salinity units). This parameterization leads to a substantial reduction of the vertical light penetration up to 700 km away from the mouth of the river during the high discharge regime in June.

The other major rivers within our Atlantic model domain are represented as surface freshwater and nutrient fluxes, spread over several grid points neighboring the river location, in the same manner as in previous ROMS-BEC simulations (Frischknecht et al., 2018; Lovecchio et al., 2017). These freshwater fluxes are derived from the observational data base of Dai et al. (2009) and the associated NO_3 and PO_4 fluxes are estimated from Beusen (2014).

Finally, we added forcing fields of atmospheric nitrogen, phosphorus and dust, based on the work of Mahowald et al. (2009) and assume that 3.5% of the dust constitutes iron, of which 2% is considered bioavailable. These inputs are added directly to the corresponding surface fields in ROMS. In using these fields, the atmospheric N deposition in the WTA is of the same order of magnitude as the DIN delivered by the Amazon, that is, 0.6 and 0.9 Tg N yr^{-1} respectively, while the deposition of P is substantially lower (Tables 3 and S4). For iron, atmospheric deposition is a key player in the WTA, providing almost twice the amount delivered by the Amazon: 0.07 Tg Fe yr^{-1} against 0.04 Tg Fe yr^{-1} for the river.

2.3. Simulations and Analyses

The physical core of the model was first run for 30 years, starting from rest with initial conditions for salinity and temperature derived from the World Ocean Atlas (WOA, 2013) (Garcia et al., 2013; Levitus et al., 2015). The model was forced at the surface by monthly climatologies of wind stress, net solar radiation, and of the fluxes of heat and freshwater. All atmospheric variables were derived from ERA-Interim reanalysis covering the 1989–2009 time period (Dee et al., 2011).

The coupled model, that is, including the ecology/biogeochemistry, was then run for another 20 years with the initial conditions for the physical variables taken from the first 30 years, and for the biogeochemical/ecological variables taken from different observation and model-based data sets. The main nutrients were derived from the climatology by WOA (2013), Garcia et al. (2013), and Levitus et al. (2015). DIC and alkalinity fields were interpolated from the climatology (1972–2013) of GLODAP gridded product (Global Ocean Data Analysis Project version 2, Lauvset et al. [2016]). For the biogeochemical tracers that were not available in WOA or GLODAP such as iron and DOM, we relied on results from a simulation of the ocean component of the NCAR Community Earth System Model that employs the same ocean biogeochemistry/ecosystem model, that is, CESM-BEC (Yang et al., 2017). The lateral boundary conditions at the open boundary in the South were derived from the same sources as the initial conditions with the seasonal cycle retained when available.

Table 1
Summary of the Regional Oceanic Modeling System-Biogeochemical/Ecological Module Simulations Performed for This Study

Name of the simulation	Description
NoAmazon	Base-line simulation: Amazon River is blocked
All	Standard simulation: All nutrients and DIC and Alk are delivered
NoNutr	Only DIC and Alk are delivered
NoDIN	Same as All but without DIN load
NoPO4	Same as All but without PO_4 load
NoDOP	Same as All but without DOP load
NoP	Same as All but without DOP and PO_4 loads
NoSi	Same as All but without $Si(OH)_4$ load
NoDOC	Same as All but without the input of terrestrial DOC

The concentrations of the Amazon River input and the resulting loads are given in Table S3.
Abbreviations: Alk, Alkalinity; DIC, Dissolved Inorganic Carbon.

The atmospheric forcing included seasonally varying atmospheric pCO_2 based on the climatology created by Landschützer et al. (2014) over the period from 1998 through 2011. To compute the atmospheric pCO_2, they used the dry air mixing ratio for the marine boundary layer from GLOBALVIEW-CO2 (2014), the atmospheric pressure from NCEP (Kalnay et al., 1996), and the water vapor correction from Dickson et al. (2007). The resulting climatology has an annual mean atmospheric pCO_2 over the domain of 365 μatm, corresponding roughly to the year 2006.

Of the 20 years of the coupled run, the first 14 years are considered as spin up. The last 6 years (years 15–20) were averaged and analyzed as a climatological mean state of our system.

To assess the effects of the Amazon River on the marine biogeochemistry, we performed a series of factorial simulations (Table 1), in which we systematically removed certain types of river fluxes in order to assess their relative contribution.

The *NoAmazon* simulation establishes the baseline, that is, where the Amazon River is blocked and thus supplies neither any freshwater nor any of the dissolved constituents. We compare this simulation to the *All* simulation that represents the most realistic (standard) simulation with the Amazon delivering all dissolved constituents, that is, the inorganic and organic nutrients as well as DIC, Alk, and terrestrial DOC. The *NoNutr* simulation sits in between these two simulations: The Amazon River delivers only DIC, Alk but no terrestrial DOC nor inorganic and organic nutrients. The other sensitivity simulations allow us to explore the impact of each inorganic or organic nutrient individually as well as the role of the input of terrestrial DOC on the air-sea balance of CO_2.

We focus our analyses to that fraction of the WTA that is most affected by the Amazon River. We define this region as extending from 0.5°S −24°N and 70°–30°W to capture the full extent of the plume waters based on our model results (Figure 1). Within these boundaries, we delimit 4 sub-regions, each exhibiting similar physical and biogeochemical characteristics. The estuary region corresponds to the extended mouth of the river (<150 km from the point of entry of the Amazon River). The shelf region is defined as that part of the continental margin that is shallower than 100 m, with the shelf-break marking the transition to the adjacent offshore region. The offshore plume region corresponds to the areas where the water column is deeper than 100 m and the surface salinity is lower than 35.25. The offshore waters exhibiting a salinity above 35.25 constitute then the nonplume region. We use a threshold of 35.25 instead of 35 as used in previous studies (e.g., Coles et al., 2013; Stukel et al., 2014; Subramaniam et al., 2008). This is based on our analyses showing a substantial Amazon influence up to these salinities. Lowering it to a threshold of 35 would have removed from our plume analysis an important share of the river influence. As the pathways of the plume vary seasonally, the spatial limits of the offshore plume and nonplume regions change throughout the year (Figures 1c–1f).

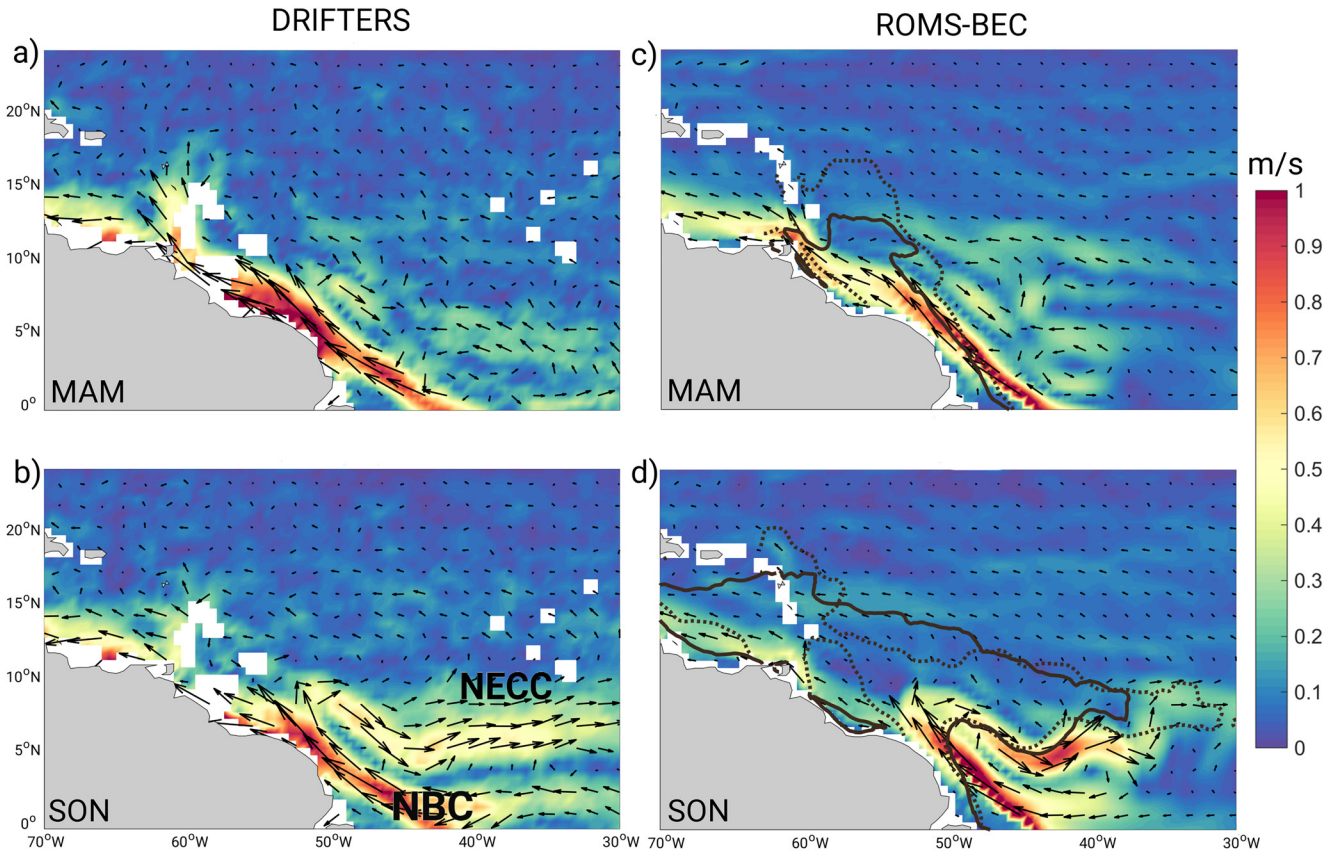

Figure 2. Maps of the seasonal mean surface ocean circulation in the Western Tropical Atlantic (WTA) (a and b) Average surface flow (m s^{-1}) in spring and fall estimated from drifters (Lumpkin & Johnson, 2013) and (c and d) in Regional Oceanic Modeling System; biogeochemical/ecological module (ROMS-BEC) (integrated in the first 15 m to be comparable to drifter data). Solid and dashed lines mark the boundaries of the plume waters ($S < 35.25$) in ROMS-BEC and in the satellite estimates (SMAP 2015–2017), respectively. The North Brazilian Current (NBC) and the North Equatorial Counter Current (NECC) are indicated in (b).

2.4. Model Evaluation

2.4.1. Circulation

The general surface circulation of the Atlantic Ocean is well reproduced by ROMS-BEC, as exemplified by the very high correlation coefficient of 0.91 between the observed and the modeled annual mean sea surface height (Figure S2). Especially encouraging is the model simulated Gulf Stream, which follows the North American coast until its branching at 40°N (Figure S3). Thus, our model does not suffer from a common bias in many ocean models in that they simulate a far too north branching of the Gulf Stream from the North American continent. The strength of the current is nonetheless underestimated by ROMS-BEC. The coarser resolution in our model in these high latitudes might impair the representation of eddies and other mesoscale dynamics, and thus temper the strength of the current. In the equatorial Atlantic, ROMS-BEC properly captures the complex structure of large scale westward currents and eastward counter currents that directly influence our region of study.

In the WTA, the model simulates the strong seasonal cycle of the currents in response to the seasonal variation of the wind field and the migration of the Intertropical Convergence Zone (ITCZ). The model captures the winter and spring dominance of the North Brazilian Current (NBC), which brings the plume waters northward along the South American continent (Figure 2). The model also represents correctly the transition to late summer and fall conditions, when the zonal equatorial currents move to a more northerly position, leading to the North Equatorial Counter Current (NECC) diverting part of the plume waters eastward (Lumpkin & Garzoli, 2005; Stramma & Schott, 1999). There are also some shortcomings. The NBC is somewhat weaker in ROMS-BEC compared to the drifter estimates (Lumpkin & Johnson, 2013). This

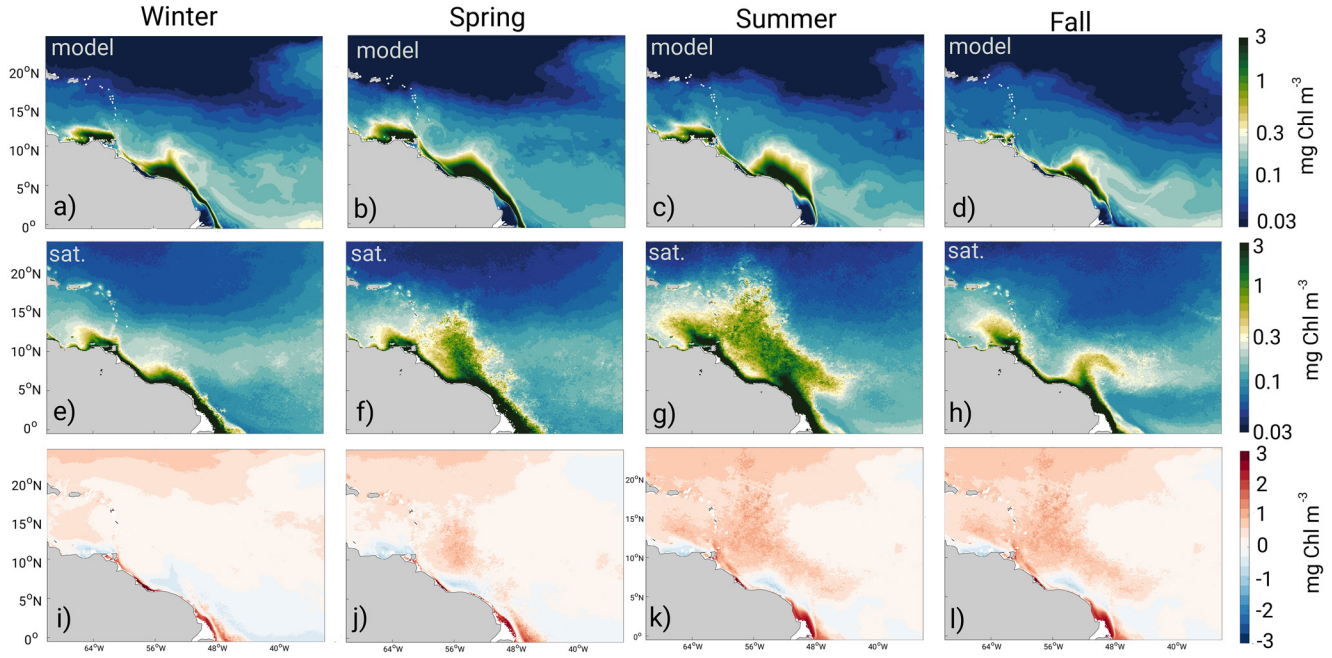

Figure 3. Maps of the seasonal mean surface chlorophyll concentration. (a–d) Average chlorophyll simulated by Regional Oceanic Modeling System; biogeochemical/ecological module (ROMS-BEC) and (e–h) estimated from sea-viewing wide field-of-view Sensor (SeaWiFS) Ocean Color Data (https://oceandata.sci.gsfc.nasa.gov/SeaWiFS/, data accessed and compiled in October 2012) (i–l) Difference between the two: SeaWiFs—ROMS-BEC. Winter is the mean of the months December through February, spring is March through May, summer is June through August and fall is September through November.

might explain that the average limit of the plume does not go as far enough north in spring as the satellite estimates indicate.

2.4.2. Biogeochemistry and Ecology

The basin-scale patterns of surface chlorophyll in the model match quite well the climatologies derived from satellite estimates (Figure S4), with a correlation coefficient of the annual mean patterns of 0.6. Despite a slight underestimation of the productivity withing the eastern boundary upwelling systems, ROMS-BEC simulates across the whole domain a NPP of 16.7 Pg C yr^{-1} which is a bit higher than the 14.6 Pg C yr^{-1} estimated by SeaWiF's Vertically Generalized Production Model (VGPM) (Westberry et al., 2008). This difference is mostly driven by the productivity in high latitudes that is stronger in the model.

In the WTA, our simulated surface chlorophyll is in good agreement with the estimates from remote sensing with an average negative bias of 0.2 mg Chl m^{-3} (Figure 3). The strongest discrepancies (locally > 10 mg Chl m^{-3}) are found very close to the mouth of the river (Figure 3). In these areas, the strength of our simulated blooms are very sensitive to the light attenuation coefficient that we apply (see Section 2.2). This is also the type of turbid waters where remote sensing algorithms generally struggle the most to differentiate the different constituents and themselves might be highly biased (Tyler et al., 2016). In general, the model reproduces the offshore gradient detected in satellite estimates, with highest surface chlorophyll concentrations in the coastal areas and lowest concentrations in the oligotrophic open ocean, north of 15°N. However, the lateral extent of the blooms, especially in summer, is somewhat cut short compared to observations. This may be caused, in part, by our too weakly simulated NBC and NECC, leading to an insufficient downstream transport of the chlorophyll-rich waters.

Although a quantitative evaluation of the major nutrients is hampered by the sparsity of the in situ measurements, the model succeeds in capturing the main seasonal and spatial variations of NO_3, PO_4 and $Si(OH)_4$ in the region (Figure 4). Following the plume pathways, riverine nutrients are transported from the mouth of the river to the open ocean, leaving a clear imprint on the spatial distribution of PO_4 and $Si(OH)_4$. In contrast, the NO_3 concentration simulated by the model remains low in the offshore plume area, in agreement with observations. In our model, this is partly caused by a substantial amount of benthic

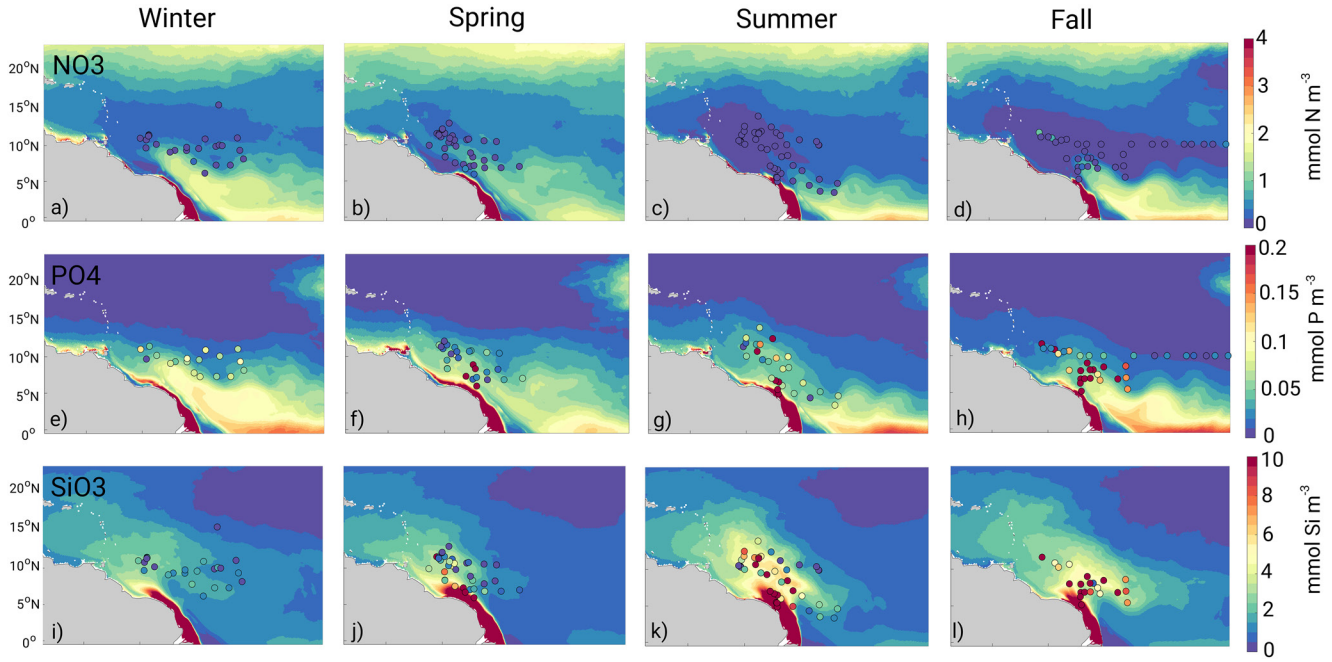

Figure 4. Maps of the seasonal mean surface concentrations of (a–d) NO_3, (e–h) PO_4, and (i–l) $Si(OH)_4$. The filled circles correspond to in situ measurements collected during several different cruises (Doherty et al., 2017; Langlois et al., 2008; Subramaniam et al., 2008). Only surface measurements are plotted (depth < 15 m). The seasons are defined as in Figure 3.

denitrification simulated to occur on the North Brazilian shelf, imprinting the waters above with a deficit of NO_3, while keeping PO_4 high. As reported in several studies (Goes et al., 2014; Subramaniam et al., 2008; Weber et al., 2017), this distinct fate of the riverine nutrients results in an excess of $Si(OH)_4$ and PO_4 over NO_3 in the offshore plume waters, with an average N:P:Si stoichiometry of 6:1:95. The area considered for this calculation exhibit a wide range of nutrient concentrations, but the concentrations are, on average, quite low: 0.2 mmol N m^{-3}, 0.04 mmol P m^{-3}, and 3.8 mmol Si m^{-3}.

ROMS-BEC simulates a total N_2 fixation over the whole basin of 26 Tg N yr^{-1}, which is at the low end of previous recent estimates: 34 ± 7 Tg N yr^{-1} (Luo et al., 2012), 46 Tg N yr^{-1} (Moore et al., 2013), and 34 [24–50] Tg N yr^{-1} (Wang et al., 2019). In agreement with field measurements that were assembled in the MAREDAT database (Luo et al., 2012), N_2 fixation in ROMS-BEC is highest in the tropical North Atlantic and then decreases from there both northward and southward (Figure S5). Around the latitude 40°N and again around the latitude 40°S, some regions exhibit a peak of total N_2 fixation before it decreases sharply toward the polar regions, due to temperature limitation in our model.

In the WTA, the measured rates of N_2 fixation are extremely variable as a result of the very dynamic hydrographic and environmental conditions. Nonetheless, Subramaniam et al. (2008) showed that some general pattern emerges and proposed to divide the area into 3 sub-regions based on sea surface salinity (SSS): low-salinity (SSS < 30), mesohaline (30 > SSS > 35) and oceanic (SSS > 35). The average rate of N_2 fixation in the study by Subramaniam et al. (2008) is the lowest in the low-salinity waters (35 ± 5 μmol m^{-2} d^{-1}) and the highest in the mesohaline waters (986 ± 373 μmol m^{-2} d^{-1}) while the oceanic waters exhibit an average rate of 157 ± 32 μmol m^{-2} d^{-1}. This general pattern is reproduced by the model with an average of N_2 fixation of 59 μmol m^{-2} d^{-1} (low-salinity), 503 μmol m^{-2} d^{-1} (mesohaline), and 152 μmol m^{-2} d^{-1} (oceanic).

2.4.3. Air-Sea CO_2 Exchange

Overall, the WTA is considered a source of CO_2 to the atmosphere (Goyet et al., 1998; Lefévre et al., 1998; Schuster et al., 2013). Except in winter, the areas that are not under the direct influence of the Amazon River (nonplume waters) are, on average, supersaturated in CO_2 with respect to atmospheric CO_2 (Figure 5c). Nevertheless, surface pCO_2 within the region exhibit a clear north south gradient (Lefévre et al., 2010; Takahashi et al., 2009) which is well captured by the model (Figure S6). The south of the domain (south of 11°N)

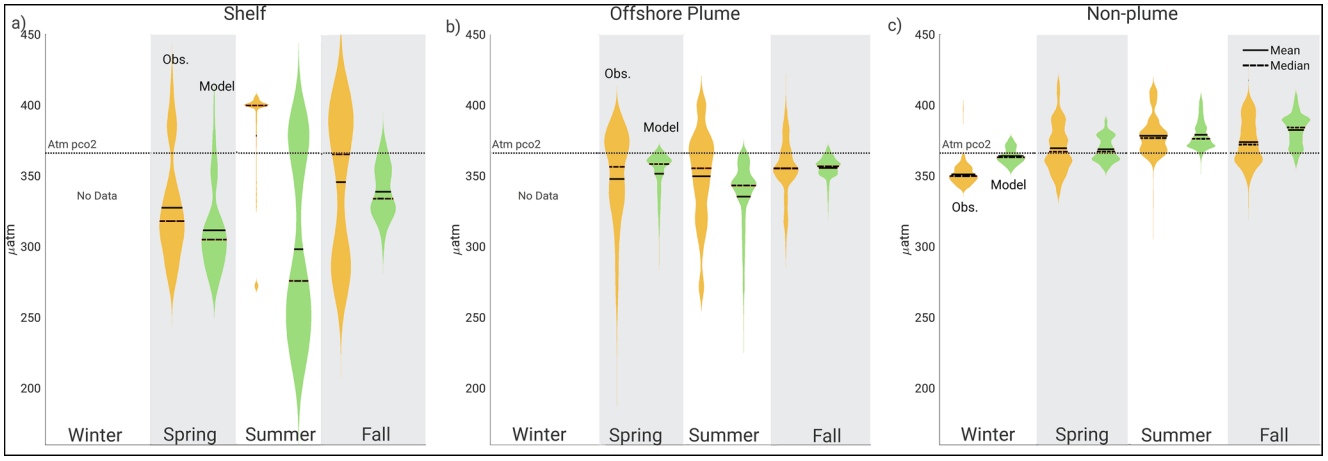

Figure 5. Evaluation of the surface ocean pCO_2: Depicted in this violin plot are the observations (yellow) and the results from Regional Oceanic Modeling System; biogeochemical/ecological module (ROMS-BEC) (green) for every season (a) over the shelf area (b) in the offshore plume waters and (c) in the nonplume waters. The shape of the plots corresponds to the kernel density, the solid line to the mean and the dashed line to the median. The dotted line is the mean atmospheric pCO_2 within the domain. Observations are derived from the ungridded Surface Ocean CO_2 Atlas (SOCAT version 2020). All data (1970–2019) have been normalized to the year 2006 and concatenated by region and seasons. The model was sampled at the same locations as the observations. The seasons are defined as in Figure 3.

displays higher surface pCO_2 than further north due to the supply of CO_2 rich waters from below by the equatorial upwelling (Lefèvre et al., 2014).

Under the influence of the Amazon River, the shelf and offshore plume waters are, on average, undersaturated with regard to atmospheric CO_2, in agreement with observations (Figures 5a and 5b). Except in the summer on the shelf, where data are too scarce to draw a conclusion, ROMS-BEC successfully reproduces the mean conditions, with mean biases less than 16 µatm. Nevertheless, the simulated pCO_2 has much less variance compared to the observations, especially in the offshore plume region. The model might underestimate the full spectrum of the pCO_2 variations owing to it being forced with monthly climatological conditions, thus lacking the influence of storms and other perturbations.

3. Changes in the Biological Pump

The differences between the standard (*All*) and the *NoAmazon* simulations reveal the large impacts of the Amazon River on the marine biological pump (Table 2). This strong stimulation is foremost a consequence of the delivery of nutrients. The impact of the Amazon induced modifications of the circulation alone are relatively small (compare *All* with *NoAmazon* and *NoNutr*). Since our focus is on the role of the nutrients, and since the role of the circulation changes is small, we use the *NoNutr* as our new reference for exploring changes in NPP and export in response to the addition of the different nutrients (Sections 3.1–3.3). We first focus our analyses on the changes in NPP, and the associated export production (EP), diagnosed from the flux of particulate organic matter across 100 m depth. We then will use the factorial simulations to analyze the results more deeply.

3.1. Overview

The nutrients delivered by the Amazon stimulate NPP in the analysis region by 115 Tg C yr^{-1} (Table 2), representing an enhancement of 9%. The largest increase occurs on the shelf, with the influence of the Amazon River weakening as the waters travel from the mouth of the river to the open ocean (Figure 6a). This additional NPP increases EP by 32 Tg C yr^{-1}, representing an overproportional increase of +17%. Similar to NPP, the magnitude of the increase diminishes as the waters reach the offshore regions (Figure 6b). A noteworthy exception is the estuary zone, where NPP and EP remain low. This is because the phytoplankton in these regions remain light limited owing to the high levels of c-DOM and turbidity. This estuary zone will thus be excluded in our subsequent analyses.

Table 2
Mean Net Primary Production and Export Production in the NoAmazon NoNutr Cases and the Changes (δ NPP, δ EP) Relative to These Cases for the Different Sub-Regions and the Total Across the Western Tropical Atlantic Analysis Region (See the Methods Section for the Definition of These Sub-Regions)

	NPP [Tg C yr^{-1}]				EP [Tg C yr^{-1}]		
Simulations	Shelf	Offshore plume	Nonplume	Total[a]	Offshore plume	Nonplume	Total
NoAmazon	64	209.2	986.62	1259.9	35.4	162.7	198.1
NoNutr	60.8	201.5	966.9	1229.3	34	158.1	192.1

	ΔNPP [Tg C yr^{-1}]				Δ*EP* [Tg C yr^{-1}]		
Simulations	Shelf[a]	Offshore plume	Nonplume	Total	Offshore plume	Nonplume	Total
All—NoAmazon	23.6 (37%)	34.9 (17%)	26.1 (3%)	84.5 (7%)	12.5 (35%)	13.5 (8%)	25.9 (13%)
All—NoNutr	26.7 (44%)	42.6 (21%)	45.8 (5%)	115.1 (9%)	13.9 (41%)	18.1 (11%)	32 (17%)
NoDIN—NoNutr	18.8 (31%)	39.7 (20%)	48.8 (5%)	107.3 (9%)	13.2 (39%)	18.7 (12%)	32 (17%)
NoPO4—NoNutr	24.6 (40%)	38.4 (19%)	31.1 (3%)	94 (8%)	12.7 (37%)	16.1 (10%)	28.7 (15%)
NoDOP—NoNutr	18.6 (31%)	1.2 (0.6%)	−30.9 (−3%)	−11.2 (−1%)	6.5 (19%)	7.6 (5%)	14.1 (7%)
NoP—NoNutr	6.9 (11%)	−9.9 (−5%)	−45.9 (−5%)	−49 (−4%)	5 (15%)	6.1 (4%)	11.1 (6%)
NoSi—NoNutr	13.7 (22%)	61.6 (31%)	108 (11%)	183.3 (15%)	5.6 (16%)	10.9 (7%)	16.5 (9%)
NoAmazon—NoNutr	3.1 (5%)	7.7 (4%)	19.7 (2%)	30.6 (2%)	1.4 (4%)	4.6 (3%)	6 (3%)

Listed are the results for the standard case *All* and the different factorial simulations. The absolute values for all factorial simulations can be found in Table S5.
[a]This includes the estuary zone.

The model simulated changes in NPP and EP are substantially larger than the potential changes one would expect from the nutrient input alone. To obtain these potential changes in NPP and EP, we assume (i) Redfield stoichiometry, (ii) that the added nutrients are completely biologically consumed in the WTA and then exported to depth, and (iii) that a constant fraction of the additional NPP is exported to depth, that is, that the export ratio (*e*-ratio) is fixed. With these assumptions, the potential changes in NPP and EP expected for each nutrient $i = NO_3$+NH_4, PO_4, DON and DOP, that is, $\Delta NPP^{i,pot}$ and $\Delta EP^{i,pot}$, can be estimated as follows:

$$\Delta EP^{i,pot} = J(N_i) \cdot r_{C:N_i} \quad (1)$$

$$\Delta NPP^{i,pot} = \frac{\Delta EP^{i,pot}}{e\text{ - ratio}} \quad (2)$$

where $J(N_i)$ represents the total amount of (inorganic or organic) nutrient N_i delivered by the Amazon River. The symbol $r_{C:N_i}$ is the carbon to nutrient phytoplankton uptake ratio of the nutrient N_i. We use a constant *e*-ratio of 0.16, which reflects the average value over the whole region of study in the *NoNutr* simulation; it implies a recycling of the nutrients in the upper ocean of more than 6 times.

These potential changes of NPP and EP (crosses in Figure 7a), differ little between the addition of DIN (NO_3 + NH_4) or PO_4 as their ratio in the Amazon input is close to Redfield (Table S3). But these potential changes are much lower than the actual realized increases in NPP and EP. In the *All* simulation (Table 2), the increase of NPP exceeds the potential increase based on DIN or PO_4 at least twofold (Figure 7a) and for EP, the realized increase is a staggering quintupling of the DIN or PO_4-based potential.

This strong amplification can only be reconciled by invoking other nutrient sources. Additional inputs of 4.2 Tg N yr^{-1} and 0.6 Tg P yr^{-1} are needed. One option is that a fraction of the river-supplied dissolved organic nutrients becomes bioavailable, since they have a very large potential for increasing NPP and export (Figure 7a), larger than actually needed to close the nutrient gap. But there are also other potentially important sources of new nutrients, primarily N_2 fixation. The stronger relative enhancement of the export production relative to NPP implies an increased export ratio, that is, that a larger fraction of NPP is exported to depth. This requires changes in the phytoplankton community structure that alter the pathway of the

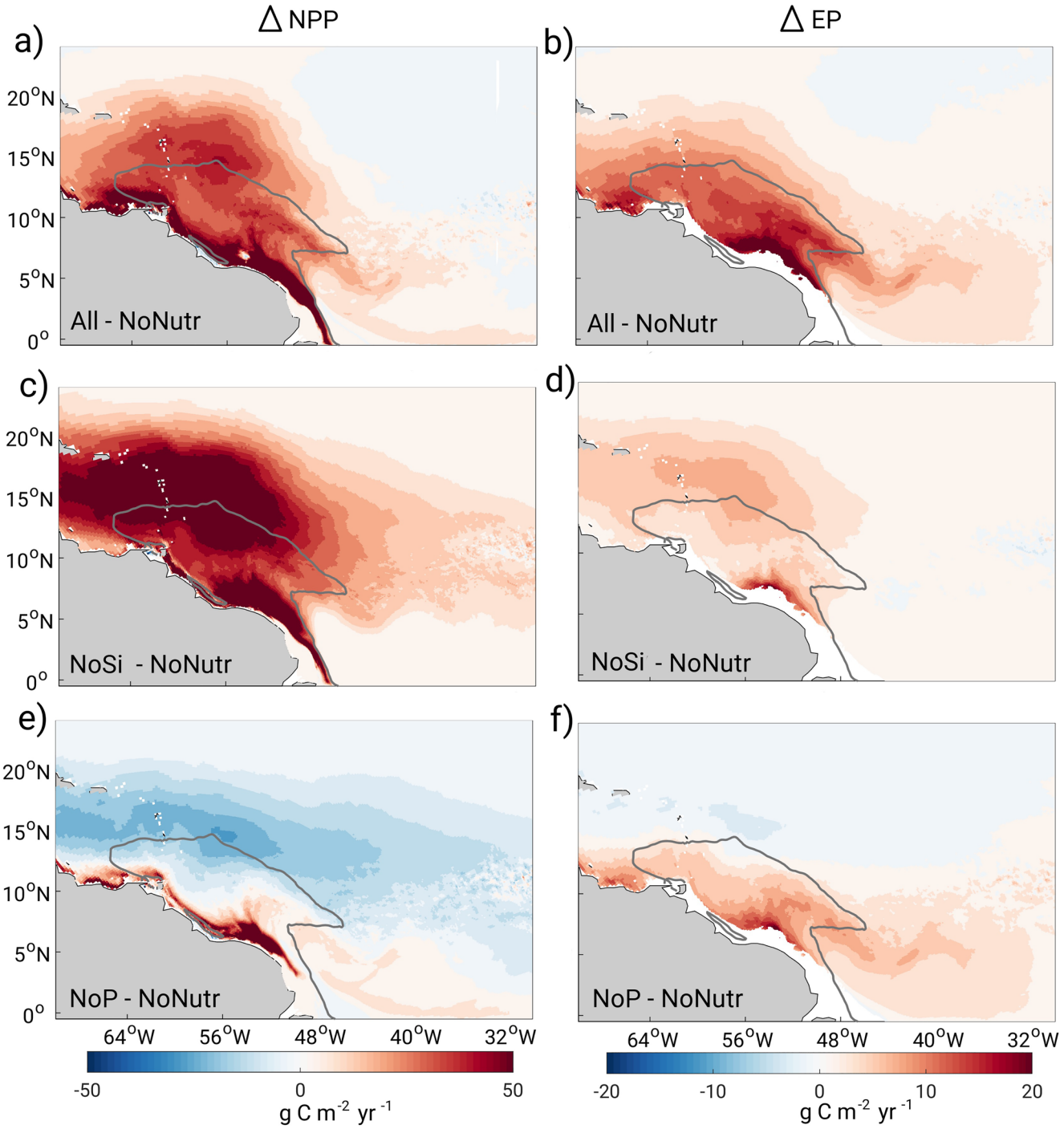

Figure 6. Maps illustrating the changes in annual mean net primary production (NPP) and export production (EP) in the western tropical Atlantic in response to the Amazon River input. (a and b) Differences between *All* and *NoNutr* simulations showing the overall impact of the Amazon on the ocean's biological pump. (c and d) Differences between the *NoSi* and *NoNutr* simulations showing the impact of all nutrients but $Si(OH)_4$. (e and f) Differences between *NoPO4* and *NoNutr* simulations showing the impact of all nutrients but PO_4. Gray lines mark the boundaries of the plume region (salinity < 35.25).

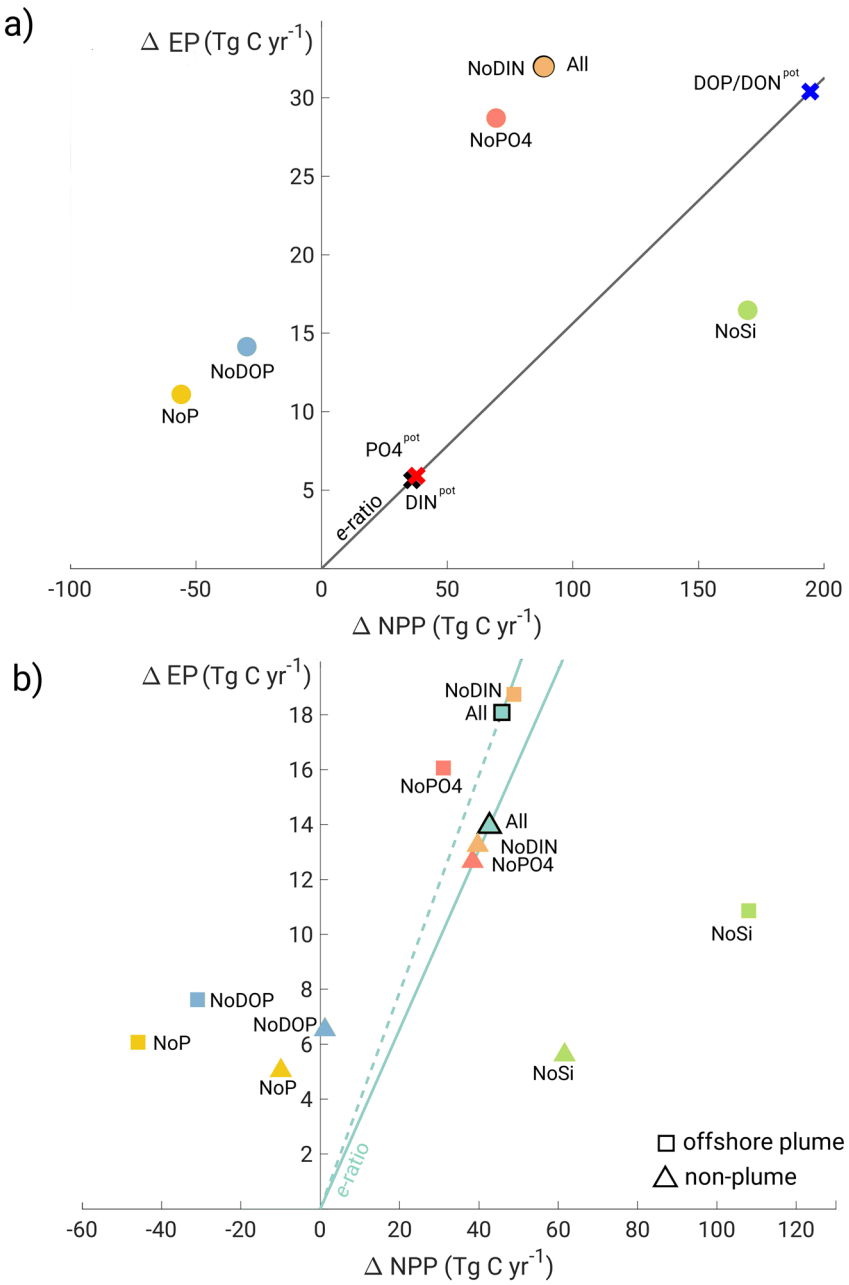

Figure 7. Relationship between the Amazon-River induced changes in NPP (integrated in the first 100 m) (ΔNPP) and the changes in export production (at 100 m) (ΔEP) for (a) the entire WTA analysis region and (b) for the individual subregions. The regionally integrated changes in production and export were computed relative to the *NoNutr* case. Shown as crosses in (a) are the potential changes in NPP and export ($\Delta NPP^{i,pot}$ and $\Delta EP^{i,pot}$), estimated based on the nutrient delivery by the Amazon (see text for further details). The line corresponds to the average e-ratio of 0.16 across the whole WTA region in the *NoNutr* simulation. In (b), the shapes represent different zones in the region (see Figure 1). The solid line and the dashed line indicate the *e*-ratio in the plume and nonplume regions, respectively, taken from the *All* simulation. In both (a and b), the colors correspond to the different simulations and will be used in subsequent figures.

fixed carbon through the upper ocean ecosystem. These results thus pose two questions: Where are the additional nutrients coming from, and what determines the changes in phytoplankton community structure that causes the increase in the *e*-ratio?

The factorial simulations, where we remove one riverine nutrient at the time, raise further questions. The omission of DIN in the Amazon River input in the *NoDIN* simulation has essentially no impact on the

Table 3
Annual Mean Sources of Inorganic Nitrogen and Phosphorus in the NoNutr and All Simulations Integrated Over the Top 100 m and the Western Tropical Atlantic

	All (Tg N yr^{-1})	*NoNutr* (Tg N yr^{-1})	Difference in %	Additional nutr. In *All* (Tg N yr^{-1})
N from river DIN input	0.9	0.0	100	0.9
N from N_2 fixation	8.9	5.1	74	3.8
N from DON remin	36	30.1	19	5.8
N from PON remin	28.1	22	28	6.1
P from river PO_4 input	0.13	0.0	100	0.13
P from DOP remin	0.0067	0.0063	7	0.0004
P from DOP uptake	3.2	2.4	34	0.8
P from POP remin	3.9	3	28	0.8

Abbreviations: DON, dissolved organic nitrogen; DOP; dissolved organic phosphorus.

biological pump within the WTA (Figure 7a). This suggests that the removal of N from the Amazon input can be easily compensated for by other sources of N, giving riverine N no limiting role for phytoplankton growth in the region. In contrast, the *NoSi* case stimulates an even larger increase of NPP than seen in the *All* simulation, but a smaller increase in EP. Furthermore, in this simulation the realized change in export falls below the average *e*-ratio line. Finally, the most perplexing results emerge from the simulations in which DOP is missing in the riverine input, that is, the *NoDOP* and the *NoP* cases. While the absence of PO_4 changes the results only somewhat, the absence of DOP leads to a decrease of NPP compared to the *NoNutr* case, even though the other nutrients are still delivered. Even more surprising is the fact that despite these decreases in NPP, EP still increases in these two simulations. These responses of the WTA to the factorial nutrient experiments highlight the fact that riverine phosphorus, and especially DOP, plays a key role in the enhancement of NPP, but that the efficiency of export, that is, the export ratio, might be driven by the presence of other riverine nutrients, namely $Si(OH)_4$.

These factorial simulations demonstrate a highly nonlinear response of the WTA to the supply of nutrients by the Amazon River. More nutrients do not necessarily translate into higher production, and there is no proportional link between river-induced changes in NPP and EP, undermining the idea that the amount of carbon exported is primarily driven by changes in NPP. This suggests strong interactions between the cycling of the different nutrient elements, with important impacts on the phytoplankton community structure, ultimately affecting the strength and efficiency of the biological pump. Thus, at least one further question emerges from these factorial simulations: How does the input of the different nutrient elements lead to these very different responses in the biological pump? In the following, we provide further results and analyses to address this question as well as the two others raised before, that is, the source of the additional nutrients and how the riverine nutrients are changing the phytoplankton community structure.

3.2. The Enhancement of Primary Production

To identify the sources of additional bio-available nitrogen and phosphorus supporting the amplification of the potential response of NPP to the addition of nutrients by the Amazon, we determine all sources of extra inorganic nitrogen and phosphorus over the upper ocean (0–100 m) of the WTA. We do this for both the *NoNutr* and *All* simulations, and then compute their difference. Since the input from the ocean and atmosphere remain essentially unchanged, we need to consider only the extra inorganic nutrient sources from (i) the riverine input, (ii) the remineralization of dissolved and particulate organic matter, (iii) N_2 fixation, and (iv) the uptake of DOP by phytoplankton (see Table 3).

For nitrogen, N_2 fixation exhibits the largest increase in relative terms between the *All* and the *NoNutr* simulations (Table 3). Over the whole WTA analysis domain, the stimulation of N_2 fixation by the Amazon River supplies an additional 3.8 Tg N yr^{-1} of new bio-available nitrogen, representing an increase of 74%. However, in absolute terms, the intensification of the recycling of organic nitrogen in the *All* simulation represents the most important source of nitrogen to the WTA with an additional flux of 5.8 Tg N yr^{-1} (DON) and 6.1 Tg N yr^{-1} (PON). While this recycling is important for NPP, it does not represent a new source. Note that we cannot a priori determine what fraction of the DON comes from terrestrial DON remineralization, since our model does not differentiate between riverine and marine-sourced DON. Nevertheless, by matching the required N to support the enhanced NPP by N_2-fixation and a fraction of the terrestrial DON remineralization, we find a fraction of about 32%. The actual percentage could be a bit higher, owing to our lack of consideration of an increase in the losses of fixed nitrogen through enhanced benthic denitrification along the North Brazilian Shelf. Thus, only a relatively small fraction of the organic N sourced inorganic N is truly new nitrogen and the N_2 fixation represents the dominant source of new nitrogen.

The recycling of phosphorus is also intensified in the *All* simulation. The remineralization of POP is enhanced by 28%, providing an additional 0.8 Tg P yr^{-1}. While the remineralization of DOP exhibits only a

small increase of 7%, adding a small amount of PO_4 (<0.001 Tg P yr^{-1}), the uptake of DOP by phytoplankton constitutes a very important source of extra phosphorus to the phytoplankton community of the WTA, providing an additional 0.8 Tg P yr^{-1}.

In summary, the large amplification of the potential response of NPP in the WTA region to the nutrient input by the Amazon River is largely supported by the strong increase in N_2-fixation that more or less doubles the total amount of new nitrogen available to fuel growth of the phytoplankton. The large addition of new nitrogen is made possible by the diazotrophic organisms having access to river supplied PO_4 and particularly to the river supplied DOP. This explains also the very different responses of NPP to the different nutrient inputs (Figures 6 and 7, Table 2). In the *NoDIN* case, diazotrophic organisms are able to nearly completely compensate for the lack of DIN input, making up for this lack by strongly enhancing their rates of N fixation. Conversely, when the input of phosphorus is lacking especially in the *NoDOP* and *NoP* cases, the diazotrophic community cannot stimulate growth and export. In fact, this community even tends to suffer in these no phosphorus cases as a result of increased competition from the other groups, leading to a reduction in NPP relative to the *NoNutr* case (Table 2).

This budget analysis resolves thus the first question about the source of the nutrients and (part of the) third question on the role of the different nutrients. But it does not answer the second question, that is, what causes the enhanced export beyond that expected by the increase in NPP, that is, what causes the increase in the *e*-ratio?

3.3. The Enhancement of Carbon Export

3.3.1. Changes in *e*-Ratios

The overall increase in the *e*-ratio across the WTA analysis region stems predominantly from the plume waters, where it increases in the *All* simulation by nearly 17% (Figure 8a). In contrast, the *e*-ratio increases by only about 6% in the nonplume waters (Figure 8b). The changes are very similar across all factorial simulations, except for the *NoSi* case, where the *e*-ratio decreases. This latter finding corresponds to the *NoSi* case lying below the potential line in Figure 7a.

To analyze the processes leading to these changes further, we split the *e*-ratio into two components: (a) the *p*-ratio, that is, the fraction of NPP that is routed to detrital POC, and (b) the *s*-ratio, that is, the sinking efficiency of POC reflecting the fraction of the total POC produced that sinks below 100 m (Laufkötter et al., 2016). This split reveals that the increase in the *e*-ratio is driven by the enhancement of the *p*-ratio, with the exception of the *NoSi* case (Figure 8). This conclusion applies to both plume and nonplume waters. In the former, this increase is slightly modified by a decrease of the *s*-ratio. In the nonplume water the *s*-ratio is almost unchanged. For the *NoSi* case, the decrease in the *e*-ratio is driven by decreases in both the s- and *p*-ratios.

Thus, in order to understand the general increase in the *e*-ratio, we need to understand what enhanced the *p*-ratio, that is, why a larger fraction of the POC produced by phytoplankton is routed to detrital POC? This routing is primarily governed by the phytoplankton community structure.

3.3.2. Phytoplankton Community Structure and POC Production

In the absence of nutrient input by the Amazon River (*NoNutr* simulation), the phytoplankton community in the plume waters is dominated by diatoms, representing 46% of the total phytoplankton community there (Figure 9). This is a consequence of upwelling at the continental shelf break supplying the $Si(OH)_4$ needed to support the growth of coastal diatoms. Small phytoplankton, already abundant in the plume waters (37%), become dominant in nonplume waters (47%), reflecting the overall the oligotrophic conditions of the open ocean WTA. The addition of nutrients by the Amazon shifts the balance strongly toward the diatoms, as the latter tend to benefit the most when nutrients are being added. In the *All* simulation, diatoms increase in the plume waters their relative share to 67% of the total biomass, while the share of the small phytoplankton drops to 18%. The same trend can be observed in the nonplume waters, although with smaller changes. The rest of the community is split between DDAs and *Trichodesmium*. Their relative importance remains more or less unaffected by the nutrient delivery by the Amazon River with DDAs dominating the diazotroph community (Figure 9).

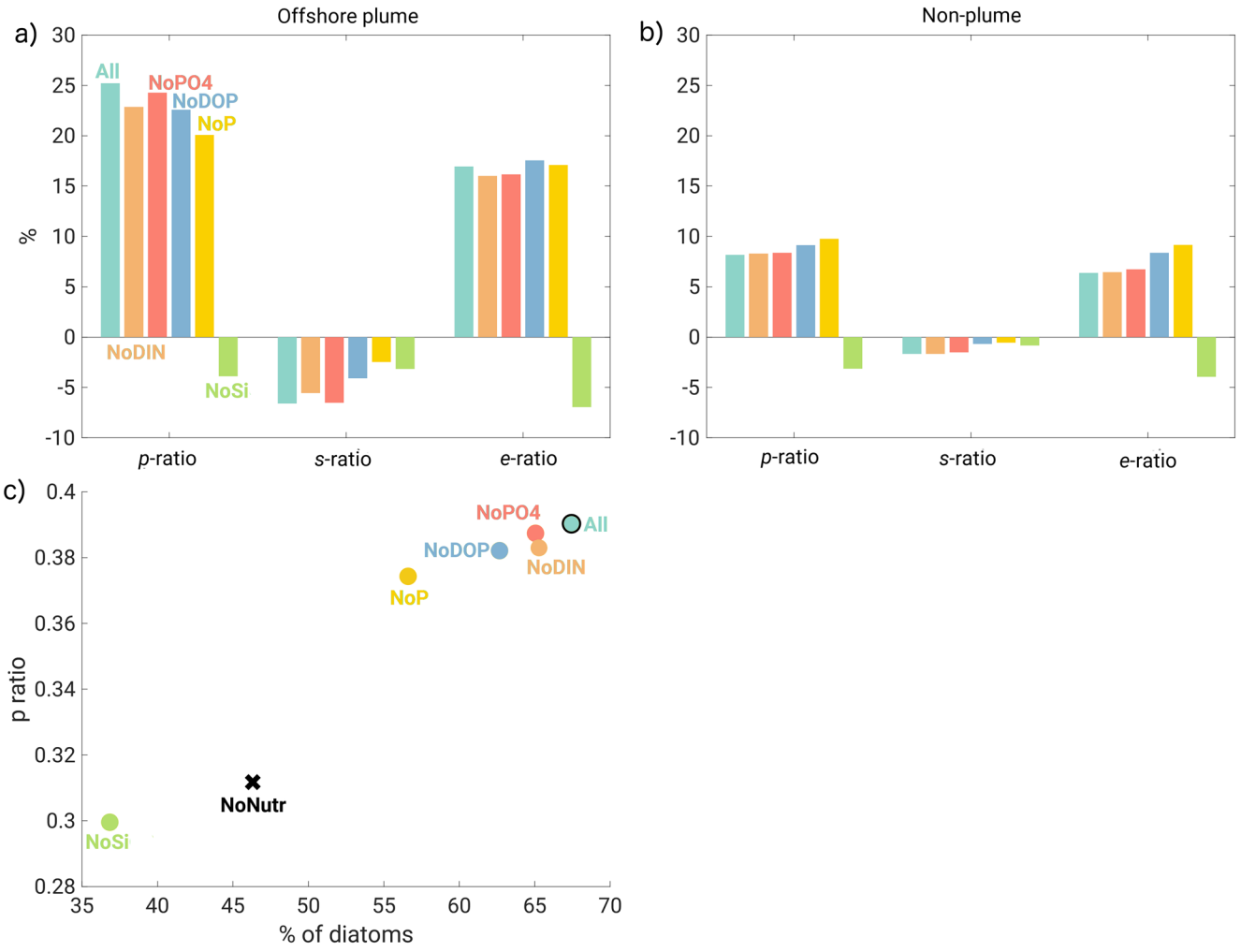

Figure 8. Amazon-river induced relative changes in the *e*-ratio and in its multiplicative factors, that is, the *p*- and *s*-ratios. Shown are the changes simulated for the *All* case and the factorial experiments relative to the *NoNutr* simulation. (a) Changes in the offshore plume waters. (b) Changes in the nonplume waters. (c) Average *p*-ratio in the plume waters as a function of the percentage of diatoms in the total phytoplankton biomass. See Figure 1 for the region boundaries.

The productivity of the different PFTs change more substantially (Figure 10). Diatoms increase their productivity very strongly, with the highest changes occurring in the plume waters. The productivity of DDAs is also boosted in most of the domain although their absolute increase is more moderate. In contrast, the small phytoplankton increase only far downstream in the nonplume waters, while they experience a decrease of their productivity in the plume waters and south of our region of study. The productivity by *Trichodesmium* does not change much. Thus, the introduction of new nutrients to the WTA benefit only some PFTs, while the others might even suffer owing to a fiercer competition between them.

The fact that diatoms, and to a lesser degree DDAs, are benefiting from the delivery of riverine nutrients is highly relevant for our analysis, since diatoms constitute the dominant pathway for the formation of detrital POC in our model, that is, they are the main PFT contributing to the high simulated *p*-ratio. In the *NoNutr* simulation, diatoms prevail in terms of POC production, even in the nonplume waters where the small phytoplankton represent the largest fraction of the community. Overall, diatoms are routing 18% and 13% of NPP to detrital POC in the plume and nonplume waters respectively (Figure 9). This flux combines the aggregate formation, the grazing loss and the nongrazing loss, but on average, more than 90% of this flux is generated by grazing. In the *All* simulation, the shift toward a diatom-dominated community translates into a larger fraction of NPP being transferred to the particulate pool, up to 28% solely through diatoms in the plume region (Figure 9).

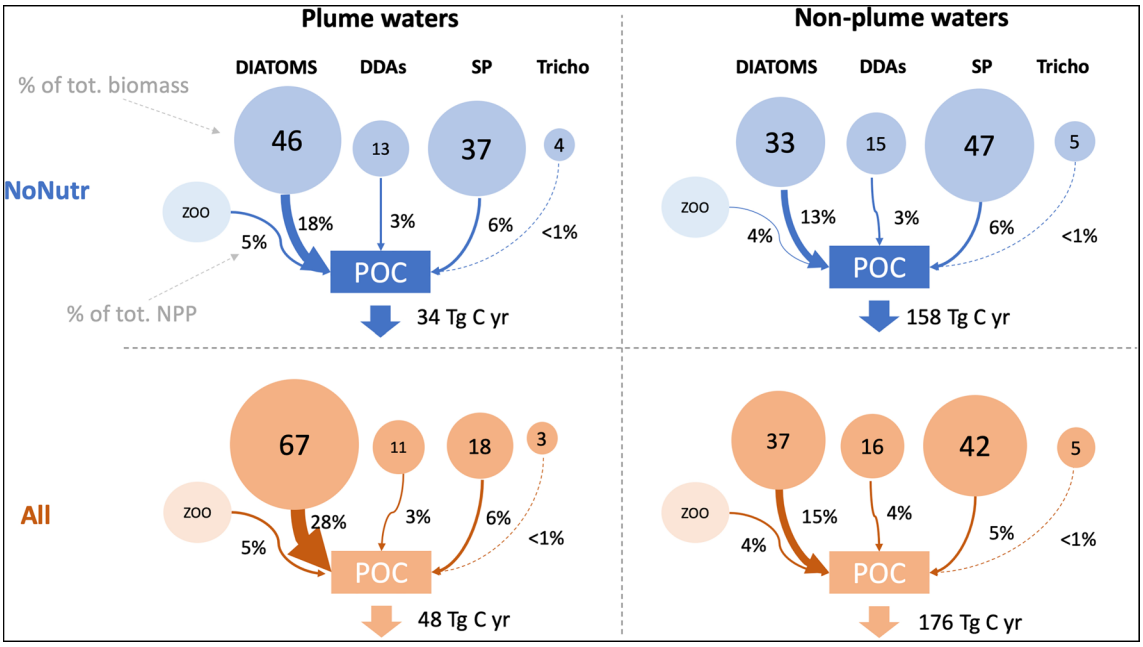

Figure 9. Phytoplankton community structure and pathways for the formation of detrital POC in the *NoNutr* simulation (top panel) and the *All* simulation (bottom panel). Indicated within each circle is the relative contribution in % of each PFT to the total phytoplankton biomass. Indicated by the arrows is the relative contribution of the different POC formation pathways associated with each PFT, given as % of total NPP in the top 100 m. The integrated POC fluxes are given separately for the plume and nonplume waters for the *NoNutr* and *All* simulations.

Thus, the prevalence of diatoms in the phytoplankton community is a key factor determining the *p*-ratio in all our simulations (Figure 8c). Overall, we can differentiate between two clusters of simulations: the simulations with a fraction of diatoms lower than 50% exhibit a *p* ratio lower than 0.32 and those with a fraction of diatoms above 55% have a *p*-ratio higher than 0.36. The first cluster gathers the 2 simulations where riverine $Si(OH)_4$ is absent.

These findings provide us now an answer to the second question we raised, that is, what determines the changes in phytoplankton community structure that causes the increase in the export ratio? It is primarily the nutrient delivery induced shift in the phytoplankton community structure toward diatoms that led to a higher fraction of NPP being exported. This shift is primarily induced by the riverine delivery of $Si(OH)_4$, which is clearly illustrated by the absence of this strong enhancement of export production in the *NoSi* case (Figure 7). The importance of diatoms in driving the *p*-ratio helps also to understand why the cases without phosphorus input, that is, *NoPO4* and especially the *NoDOP* case, have actually higher export than the *NoNutr* case, even though their NPP is smaller (Figure 7). In these simulations, diatoms become more dominant, as they end up profiting most of the extra nutrients.

3.3.3. Depth of Production and the *s*-ratio

While changes in phytoplankton community structure induced by the input of riverine nutrients explain the increase in the *p*-ratio, we have not yet addressed the possible reasons for why the *s*-ratio decreases, that is, the fraction of detrital POC that escapes remineralization within the top 100 m and thus is exported to depth (Figure 8). It turns out that this is primarily a consequence of changes in the vertical distribution of organic matter production. Given that the remineralization of detrital organic matter tends to be swift, the lesser time particles spent in the top 100 m, the larger the fraction that gets exported vertically. If the particulate matter is mostly produced at depth, the time it requires to sink out of the top 100 m is much smaller compared to a particle that is produced near the surface. The *s*-ratio is thus directly impacted by the depth profile of POC production.

In the *All* simulation, a higher fraction of the POC is produced near the surface, reflecting the fact that the lighter and nutrient-rich waters of the river plume remain near the surface (Figure 11). In contrast, the distribution of POC production in the *NoNutr* simulation is more uniform throughout the depths, implying

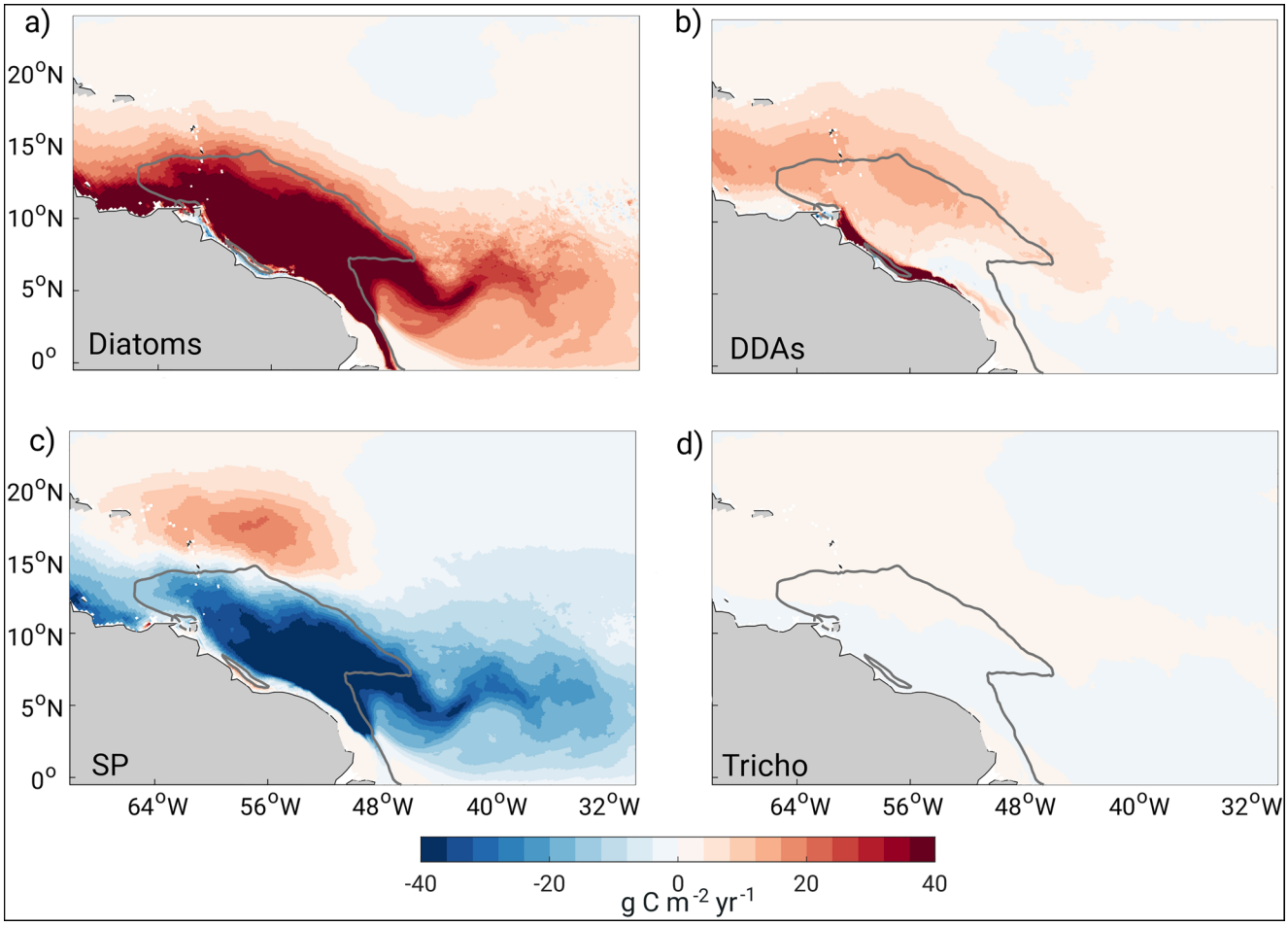

Figure 10. Maps of the changes in NPP integrated over the top 100 m in response to the nutrient addition by the Amazon River for the different phytoplankton functional types, that is, (a) the diatoms, (b) the diatom-diazotroph assemblage (DDA), (c) the small phytoplankton, and (d) the Trichodesmium groups. Shown are the differences between the *All* and the *NoNutr* simulations.

in relative terms that a smaller fraction of the total POC is produced atop the water column compared to the *All* simulation. The same is true for the factorial simulations. The *NoP* simulation in which the depth profile of POC production resembles the *NoNutr* case shows the smallest change in *s*-ratio. In contrast, the depth profile of POC production *NoPO4* simulation is close to the one in the *All* simulation and their changes in terms of *s*-ratio are similar.

Overall, our results suggest that the fate of the additional carbon that is fixed in response to the delivery of riverine nutrients depends for the most part on the phytoplankton community structure that drives the production of particulate matter. To a lesser extent, the vertical distribution of the POC production influences what fraction of the POC pool sinks below 100 m and thus modulates the efficiency of the export measured by the *e*-ratio.

4. Changes in the Air-Sea CO_2 Balance

The strong stimulation of the ocean's biological pump pushes the air-sea CO_2 balance of the WTA toward a sink, aided also by the riverine input of Alk. But the supply of large amounts of DIC and of terrestrial DOC by the Amazon tends to cause ocean outgassing, thus offsetting the biological sink. Therefore, it is the balance between this set of processes that will determine the overall balance. To account for these different processes, we use the *NoAmazon* simulation here as our reference, as only the latter does not account for the riverine input of DIC and Alk.

Table 4
Annually Integrated CO_2 Fluxes

Sub-regions	*All* (Tg C yr^{-1})	*NoDOC* (Tg C yr^{-1})	*NoNutr* (Tg C yr^{-1})	*NoAmazon* (Tg C yr^{-1})	Total effect of Amazon (Tg C yr^{-1})
Estuary	1.5	1.3	1.1	−0.2	1.7
Shelf	−3.7	−4.2	−2.3	0.7	−4.5
Offshore plume	−4.7	−7.6	1.5	6.1	−10.8
Nonplume	26.2	18.9	34.8	39.2	−13
Total Western Tropical Atlantic	19.3	8.4	35.1	45.8	−26.5

Negative values correspond to an uptake of CO_2 by the ocean and positive values correspond to outgassing. The boundaries for the sub-regions are taken from the All simulation and shown in Figure 1.

4.1. Air-Sea CO_2 Balance of the WTA

In the *NoAmazon* case, the WTA analysis region ($A = 9.6 \times 10^6$ km^{-2}) is a big source to the atmosphere, releasing 45.8 Tg C yr^{-1} of CO_2. Some of the coastal areas exhibit a modest uptake (<0.5 mol C m^{-2} yr^{-1}), most likely related to the presence of the Orinoco River and small-scale upwellings stimulating primary and export production. However, the majority of the WTA in this simulation releases CO_2, except for a latitudinal band around 12°N in the western part of the region that is close to balance (Figure 12a).

The Amazon River in the *All* simulation reduces this CO_2 outgassing over the whole region by a factor of two to 19.3 Tg C yr^{-1}. The air-sea CO_2 fluxes also become spatially more variable, with strong source and sink regions (Figure 12b). The Amazon's estuary becomes a strong source of CO_2 to the atmosphere. Despite its small size, this area alone is responsible for an outgassing of 1.5 Tg C yr^{-1}. In contrast, the shelf waters become a sink of 3.7 Tg C yr^{-1}. The intensity of this sink is highest close to the estuary zone and decreases as the waters travel northwards (Figure 12b). The transition between the outgassing estuary and the undersaturated shelf is very sharp and corresponds to the area where the improvement of the light conditions allows for high primary production to set in (Figure 6). The offshore plume waters also become a sink for atmospheric CO_2. Even though the intensity of the uptake is smaller than in the shelf waters, this region is responsible for an uptake of 4.7 Tg C yr^{-1}, representing the largest sink of our study area (Table 4). The nonplume waters, in contrast, are a net source of 26.2 Tg C yr^{-1}.

4.2. Factors Contributing to the Air-Sea CO_2 Balance

The factorial simulations permit us to disentangle the different mechanisms controlling the response of the air-sea CO_2 fluxes to the input of nutrients and carbon by the Amazon River (Figures 12c-f). The difference between the *All* and *NoAmazon* simulations reflects the net effect of the Amazon River (Figure 13). In the estuary waters, the net effect is a change of 1.7 Tg C yr^{-1} from a slight uptake in the *NoAmazon* simulation to an outgassing in the *All* simulation. In the shelf and plume waters, the presence of the Amazon River turns the slight outgassing of CO_2 in the *NoAmazon* simulation to a strong uptake, resulting in a net change of −4.5 and −10.8 Tg C yr^{-1}, respectively. In the nonplume waters, the net effect of the Amazon River comes to −13 Tg C yr^{-1}, reducing the outgassing of this vast region.

To quantify the contribution to the different factors leading to this total effect, we computed the differences between the simulations for each region as follows: (a) *All* - *NoDOC* to investigate the changes in air-sea CO_2 fluxes due to the delivery of terrestrial DOC, (b) *NoDOC* - *NoNutr* to explore the changes due to the alteration of biology, as a response of the riverine nutrient inputs, (c) *NoNutr* - *NoAmazon* to assess the remaining mechanisms affecting the air-sea CO_2 fluxes such as the impact of the riverine delivery of DIC and Alk, and the impact of freshwater on ocean stratification and circulation (Figure S7). Unfortunately, we cannot disentangle these two effects in our factorial simulations. The consideration of another factorial case with only freshwater input would not solve this issue, since the addition of freshwater without any DIC or Alk would lead to an undesired strong dilution effect.

The addition of terrestrial DOC in the marine realm causes a substantial outgassing (Figure 13), reflecting the relatively fast breakdown of this organic matter to produce DIC that then drives a flux of CO_2 out of

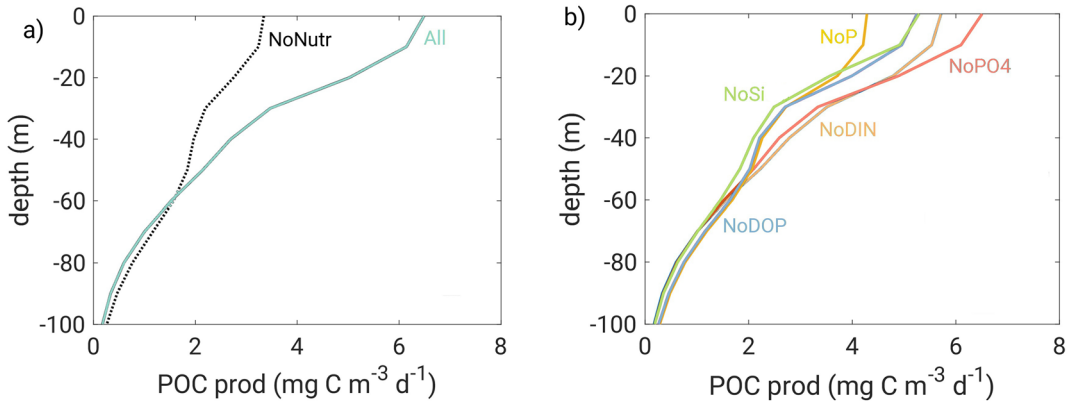

Figure 11. Annual mean rate of detrital particulate organic carbon production in the plume waters as a function of depth (a) in the *NoNutr* and *All* simulations, and (b) in all other factorial simulations.

the ocean. The relative importance of this outgassing increases when moving from the estuary to the open ocean. In the nonplume waters, the terrestrial DOC promotes a CO_2 release of 7.3 Tg C yr^{-1}.

The effect of the river input of DIC and Alk and the physical alteration due to the input of freshwater is largest in the estuary and on the shelf. In the estuary, the river supply of waters that have almost no excess of Alk over DIC (Sarmiento & Gruber, 2006) creates a very high pCO_2 (up to nearly 700 μatm in June) leading to a strong CO_2 outgassing (Figure 13). The high pCO_2 is only minimally offset by CO_2 uptake by phytoplankton growth owing to the high turbidity of the waters in this region impeding it. On the shelf, as the plume travels northward, the river waters mix with marine waters that have a relatively high excess of Alk over DIC, reducing pCO_2. As the waters clear up (around a salinity of 25), primary production sets in, lowering pCO_2 even further. In the nonplume waters, the changes are relatively small (around 4 Tg C yr^{-1}), for reasons we cannot firmly establish.

The biggest effect of the Amazon induced changes in the air-sea CO_2 balance stems from the biological carbon pump driving a very substantial uptake of CO_2 from the atmosphere. A key reason for this strong impact is that most of the increase of NPP and POC production occurs rather shallow in the water column (Figure 11), thereby increasing the fraction of CO_2 that is taken up from the atmosphere as opposed to taken from the water column (see Table S6, and e.g., Jin et al. [2008] for a discussion of this atmospheric uptake efficiency). Thus, in addition to the nutrient supply, the enhancement of stratification by the Amazon River (Pailler et al., 1999) associated with a nutrient-rich discharge makes the plume waters especially efficient in taking up atmospheric CO_2.

Overall, our results suggest that in the areas close to the mouth of the river, the riverine carbonate chemistry has the largest impact on the air-sea CO_2 balance, driving the outgassing in the estuary zone and enhancing the uptake in the shelf region. Further off shore in the plume and nonplume regions, the biological changes induced by the riverine nutrients play the leading role.

5. Caveats and Limitations

Our modeling work comes with several limitations that are inherent to the model structure and parameters choices. Our biggest limitations are associated, perhaps, with the handling of organic matter in BEC, both particulate and dissolved. The routing of particulate organic matter through the ecosystem has been shown to differ a lot between biogeochemical models and significantly impact the magnitude of particle formation (Laufkötter et al., 2016). Particularly relevant is the role of diatoms. While we account for this in our parameterizations, we treat DDAs and normal diatoms the same way, even though DDAs have been hypothesized to be more efficient in this export (Korte et al., 2020). This means that we may tend to underestimate the contribution of DDAs to POM formation and EP. A further consideration is the treatment of grazing. With BEC having only one grazer, this provides very limited capability to implement variations in grazing pressure, with implications for the phytoplankton community structure.

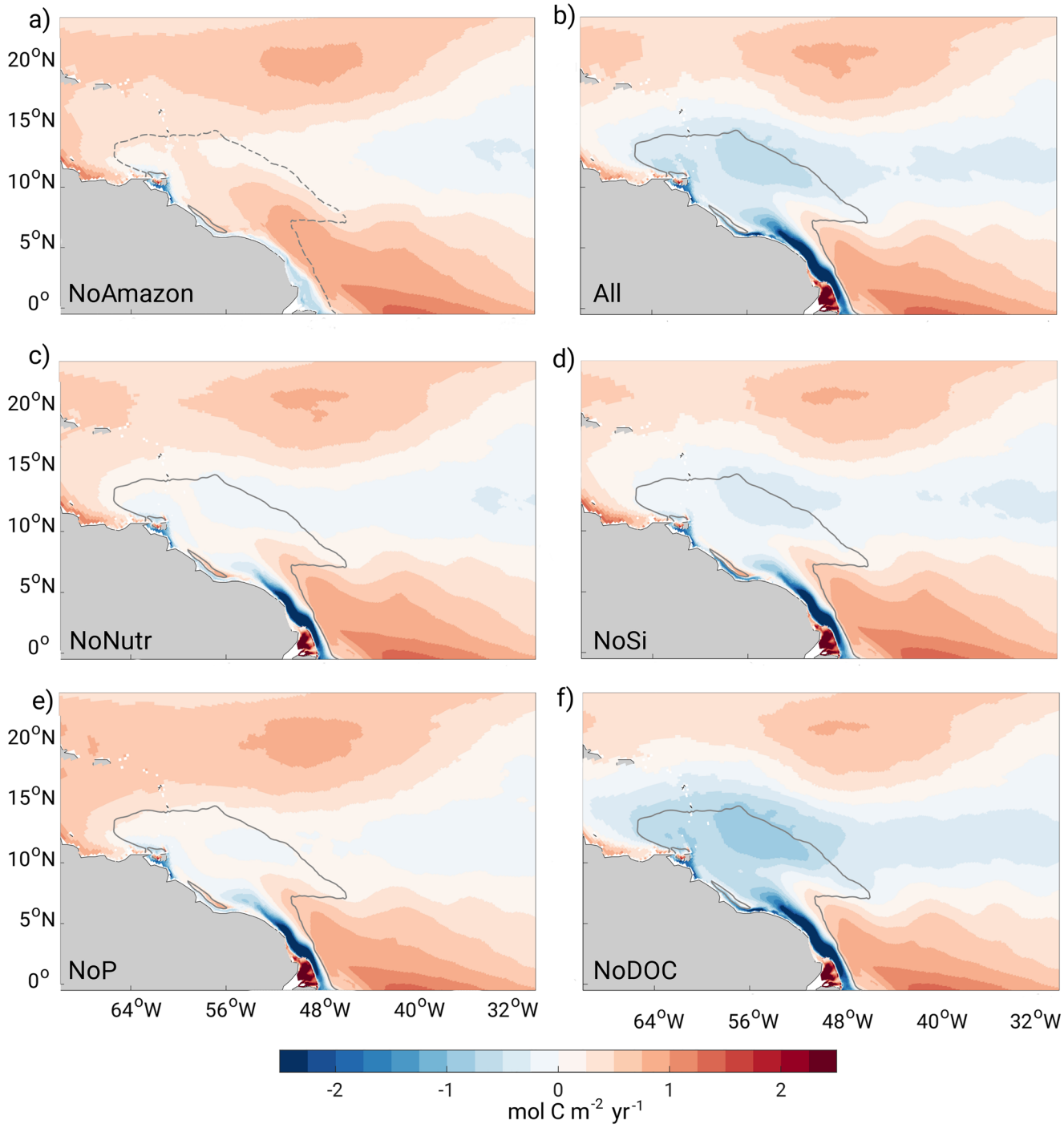

Figure 12. Maps of the model simulated annual average air-sea CO_2 flux density in the Western Tropical Atlantic (mol C m^{-2} yr^{-1}). Shown are the fluxes (positive outgassing) from (a) the *NoAmazon* case, (b) the *All* case, (c) the *NoNutr* case and (d) the *NoSi* case, (e) the *NoP* case, (f) the *NoDOC* case. See Table 1 for a description of the different cases. The solid lines in each panel correspond to the average plume limits.

Our results are also sensitive to our assumptions regarding DOM. We chose to apply a canonical Redfield stoichiometry to estimate the concentration of the terrestrial DON and DOP delivered by the Amazon. While our results are insensitive to DON, they are sensitive to our assumptions about terrestrial DOP. Using a limited number of DOP measurements, Richey et al. (1991) suggested a riverine DOP concentration of about 0.5 mmol P m^{-3}. Thus, our estimate of 4 mmol P m^{-3} is on the high side. This would imply that we

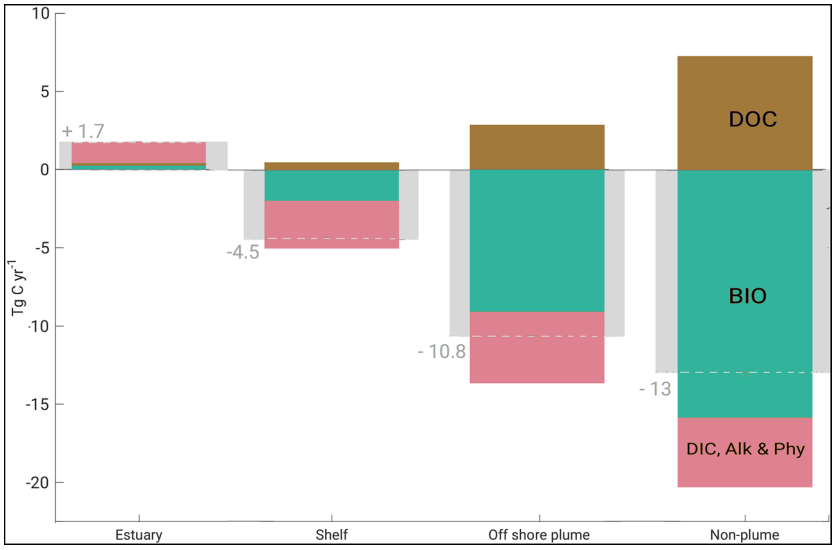

Figure 13. Quantification of the different factors contributing to the total effect of the Amazon River on the air-sea CO_2 fluxes in different regions. Pink corresponds to the effect of the river input of freshwater, Dissolved Inorganic Carbon (DIC), and Alkalinity (Alk). Green reflects the contribution of the biological pump, and brown represents the outgassing driven by the riverine input of terrestrial DOC. The gray bar and associated values highlight the total net effect of the Amazon.

may have overestimated the DOP stimulated N_2 fixation and consequently also primary production. On the other hand, our model misses other P sources such as the desorption from particulates, which has been suggested to be significant (Berner & Rao, 1994).

Other choices likely to affect our results are the nondifferentiation between terrestrial and marine DOM and the parameters driving the lifetimes of the different components of DOM. These aspects of DOM dynamics are critical in controlling where along the plume pathway regenerated nutrients and inorganic carbon are supplied back to the system. However, given the paucity of data to constrain the potential parameters, we did not implement terrestrial DOM pools in BEC to avoid adding unconstrained complexity. In this regard, more in situ/experimental studies unraveling the dynamics of the DOM delivered by the Amazon, especially DON and DOP would be very valuable.

The simulated nutrient dynamics and associated response to the Amazon inputs might also be affected by our decision to close the lateral boundaries in the Arctic and within the Mediterranean. Indeed, the Arctic Ocean inflow into the North Atlantic is associated with a low N:P ratio (Torres-Valdés et al., 2013) that we do not capture. But we expect this effect to be small owing to the short time-integration of our model, resulting in a smaller influence of the lateral boundary conditions in our simulations. Coles and Hood (2006) showed that the inflow of the high N:P waters from the Mediterranean has a significant effect on the basin-wide N:P stoichiometry and might lead to an overestimation of simulated N_2 fixation if this inflow was not represented in the model. But while the closed boundary within the Mediterranean implies that we do not restore the nutrients there toward observations, our model includes the Mediterranean outflow and thus includes a mechanism to carry the high N:P waters of this basin into the Atlantic. We therefore do not expect our decision to close the Mediterranean boundary to impact our results substantially.

Despite the limitations described above, our estimates of EP and air-sea CO_2 fluxes match quite well previous estimates based on observations (see Section 6), giving us confidence that most of our conclusions are robust.

6. Comparison to Previous Work

Our estimate of the amount of extra NPP fueled by the input of nutrients by the Amazon is comparable in magnitude to that reported by Da Cunha and Buitenhuis (2013), especially when considering that their estimate included the enhancement from all the rivers of the region. They simulated an increase of NPP of 34% (140 Tg C yr^{-1}) in the coastal tropical Atlantic Ocean (20°S–20°N, 70°W–20°E), close to our value of 9% (115 Tg C yr^{-1}). In contrast, Lacroix et al. (2020) estimated a much larger increase of NPP, that is, they found an enhancement of +166% in the Amazon shelf area (<250 m deep). But they also noted that in their simulations, the sink of nutrients in coastal areas might be too large.

Our finding of the Amazon River strongly stimulating N_2 fixation in the WTA is supported by numerous observational studies (DeMaster et al., 1991; Subramaniam et al., 2008). In fact, the region downstream of the Amazon is globally one of the regions with the highest N_2 fixation rates (Luo et al., 2012). In comparison, in their modeling study, Da Cunha and Buitenhuis (2013) found a much smaller increase of only +0.28 Tg N yr^{-1}. They considered only a single canonical diazotrophs, while the additional consideration of DDAs in our study might explain this difference. DDAs, having a higher growth rate than regular diazotrophs (Table S1), are more prone to develop large blooms.

In line with Sohm and Capone (2010) who highlighted an elevated turnover of PO_4 in the WTA characteristic of a P deficiency, phosphorus is the key limiting nutrient in our simulations. This situation is only reinforced by the fact that the atmospheric deposition influx is dominated by N compared to P (Chien et al., 2016). This makes the magnitude of the river supply of PO_4 and DOP the most important controls on how the Amazon impacts the WTA. Terrestrial DOP plays a special role in our model, given its direct uptake by diazotrophs and their role in stimulating further production.

Overall, the presence of the Amazon River is responsible for an increase of POC export at 100 m of 32 Tg C yr^{-1}, which is close to the estimate of 27.6 Tg C yr^{-1} estimated by Subramaniam et al. (2008). However, Subramaniam et al. (2008) attributed 70% of this POC export increase to DDAs, whereas our results indicate only a 15% contribution and a much larger contribution by diatoms (70%). For their calculation, Subramaniam et al. (2008) extrapolated their estimate of C-fixation from DDAs, thus assuming the same level of production over all the mesohaline waters (salinities of 30–35). This might have led to an overestimation of the importance of DDAs that represent 28% of the total biomass in their sampled stations. In our simulations, even if the productivity of DDAs substantially increases due to riverine inputs, their relative contribution to the total biomass is only 11% in offshore plume waters. This is in line with the simulation performed by Stukel et al. (2014), where DDAs contributed to 10% of the total biomass.

In our simulations, although DDAs play a key role in providing additional nitrogen to the system and contribute significantly to the export of carbon depths, they do not represent the main pathway for the transfer of carbon to depth. This role is taken by diatoms. This is consistent with many observations, while Korte et al. (2020) recently provided sediment trap-based evidence that suggested that DDAs might be more efficient at transferring carbon at depths than regular diatoms. If this was a general pattern, it would increase the importance of DDAs in our simulations.

Our study confirms the hypothesis put forward in several studies (Araujo et al., 2014; Cooley et al., 2007; Subramaniam et al., 2008; Yeung et al., 2012) that the CO_2 undersaturation in the offshore plume waters is a result of an enhancement of the biological pump by the Amazon River. In the *All* simulation, the offshore plume waters constitute a sink of atmospheric CO_2 of 4.7 Tg C yr^{-1}. Our estimate is in the range of previous assessments, with earlier studies having estimated a larger sink [Körtzinger, 2003: 14.5 (±5) Tg C yr^{-1}, Cooley et al. (2007): 15 (±6) Tg C yr^{-1}] than more recent ones (Lefévre et al. (2010): 5 Tg C yr^{-1}, Ibánhez et al. (2017): 7.85 (±1.02) Tg C yr^{-1}). The exact contribution of biology is rarely elucidated. Ternon et al. (2000) determined that primary production could contribute to 30% of the CO_2 undersaturation, while Cooley et al. (2007) estimated that it could enhance the undersaturation by 100%. In our simulations, 60% of the net effect of the Amazon River can be attributed to changes in biology within the offshore plume waters. Our results also show that the impact goes well beyond the plume waters, with the enhanced biological pump creating an anomalous sink in the offshore nonplume waters that is less intense, but integrates to a similar net sink as that realized in the plume waters.

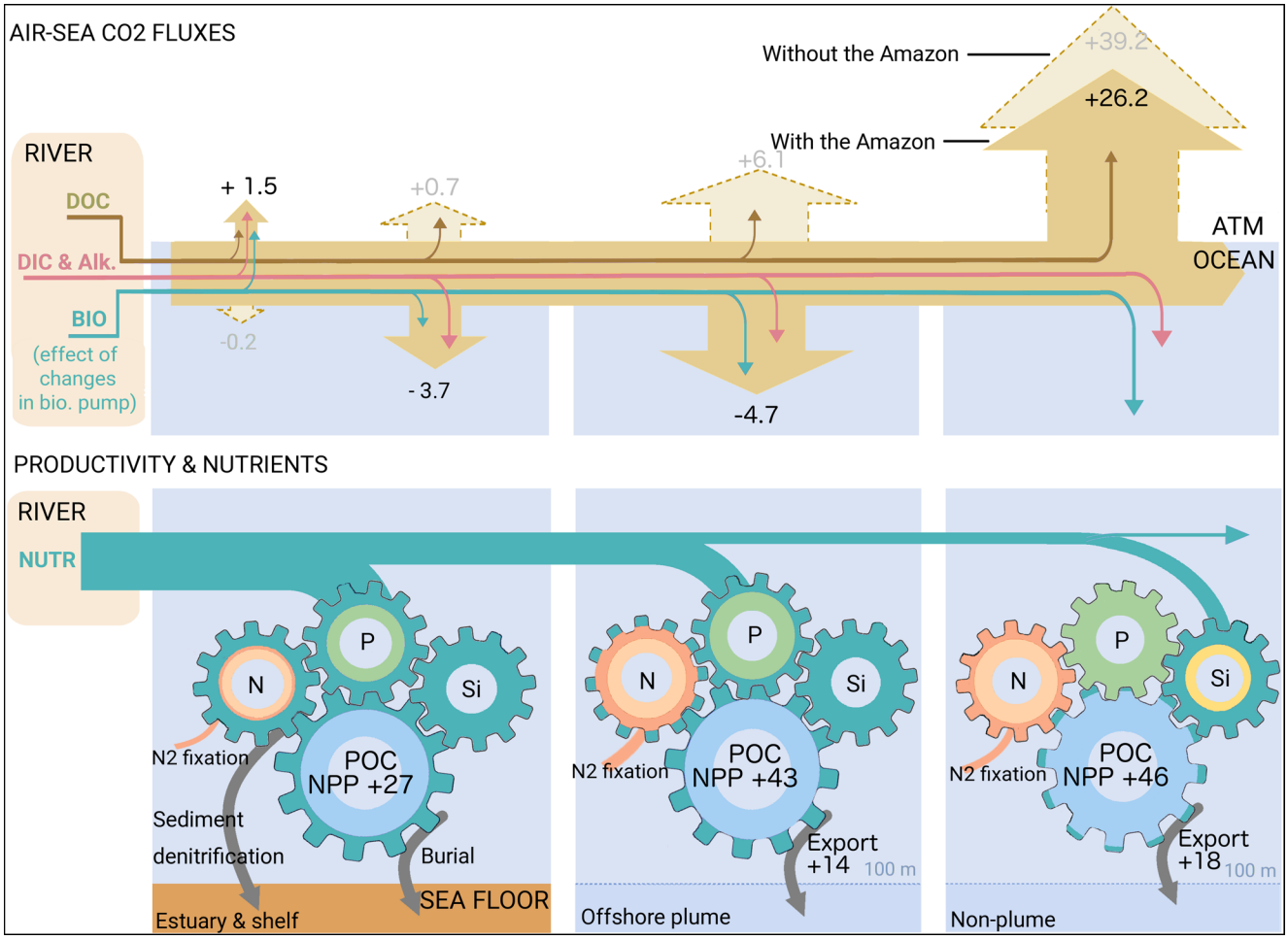

Figure 14. Schematic summarizing the impacts of the Amazon on the biological pump, the cycling of nutrients, and the air-sea CO_2 balance. The top yellow arrows represent the air-sea CO_2 fluxes. The solid one corresponds to the *All* simulation while the dashed one represents the *NoAmazon* case. The smaller arrows inside illustrate the effect of the different riverine inputs on the air-sea CO_2 exchange. The cogs represent the cycling of different nutrients with their riverine fraction indicated in green and the marine fraction in a different color: orange for NO_3, light green for PO_4, blue for POC and yellow for $Si(OH)_4$. All values are the climatological annual mean fluxes in Tg C yr^{-1}.

In all regions, the remineralization of terrestrial DOC drives an outgassing of CO_2. But the magnitude of this effect in in our model is smaller than hypothesized in a previous study (Lefèvre et al., 2017, and references herein). However, Medeiros et al. (2015) showed that a large fraction (between 50% and 76%) of the Amazon River DOM was stable in the coastal ocean. This corresponds roughly to our results, which are, of course, strongly dependent on the chosen remineralization time-scale of DOC.

7. Summary and Synthesis

The Amazon River has a substantial and cascading impact on marine biogeochemistry, the biological pump, and the air-sea CO_2 of the WTA, which we synthesize in Figure 14. In the top panel, we illustrate the overall effect of the Amazon on the air-sea CO_2 fluxes and the different controlling factors. The Amazon induces an additional outgassing of 1.7 Tg C yr^{-1} in the nearshore areas, but creates an additional uptake of 28 Tg C yr^{-1} in the remaining of the WTA, as illustrated by the differences between the large yellow arrows. Most importantly, the Amazon leads to a reversal of the outgassing in the shelf regions and in the plume waters, making these regions net sinks for atmospheric CO_2. This is the combined result of the delivery of nutrients, organic and inorganic carbon, alkalinity and low salinity waters, most of them acting in concert, but not always.

Our factorial experiments permitted us to demonstrate that the Amazon-induced enhancement of the ocean's biological pump is the main driver for this enhanced uptake (green arrow in the top panel). But our study underlines the nonlinearity of this causal chain and the importance of internal feedbacks. In the bottom panel of Figure 14, we represent the distinct types and ranges of impacts that the riverine nutrients have on the different nutrients and carbon cycles. Overall, NPP increases in response to the nutrient inputs by the Amazon by 115 Tg C yr^{-1} and EP by 32 Tg C yr^{-1}. Riverine phosphorus (light green cog) plays a key role in supporting the increase in primary productivity. The ambient marine waters are highly depleted in inorganic phosphorus and any addition of riverine PO_4 is bound to translate into more productivity, in an almost proportional fashion. Even more crucial is the role of DOP whose direct use by diazotrophs is necessary to sustain their blooms. In contrast, the delivery of inorganic nitrogen does not affect the entire system very much. N_2 fixation and additional regenerated nitrogen dominate the nitrogen sources and allow NPP to increase way beyond what the total consumption of riverine DIN can support, as illustrated by the rapidly decreasing fraction of riverine N in Figure 14. Riverine $Si(OH)_4$, on the other hand, is not completely consumed within the WTA and part of it escapes our region of study. Predominantly, $Si(OH)_4$ modulates the NPP to export relationship. Its presence results in a shift in the phytoplankton community from a small phytoplankton dominated community to a diatom-dominated community, enhancing the efficiency of the biological pump. By sending more carbon and nutrients to depths, the presence of riverine $Si(OH)_4$ also reduces the recycling of nutrients in the euphotic zone and ultimately tempers the enhancement of primary productivity.

The DIC and Alk concentration of the river waters (pink arrows in Figure 14) and the delivery of terrestrial DOC (brown arrows) are mostly affecting the regions close to the mouth of the river (estuary and shelf waters). More than the absolute amounts of DIC and alkalinity, it is the ratio between the two that affects the air-sea CO_2 balance the most, pushing the system toward oversaturated or undersaturated conditions. Regarding terrestrial DOC, our results are sensitive to its lability that will determine where it will be remineralized, counteracting the effect of the biological pump. In our simulations, the contribution of DIC, alkalinity and terrestrial DOC to the changes in air-sea CO_2 fluxes remains significant further offshore, with a clear downstream effect (Figure 14). The effect of the Amazon beyond the physical structure of its plume is small in relative terms but our results show that the impact can be substantial when integrated over such a large area.

Data Availability Statement

Model output data are available online in the ETH library archive (https://doi.org/10.3929/ethz-b-000437973) and may alternatively be obtained upon request (domitille.louchard@usys.ethz.ch).

Acknowledgments
This study was part of the C-CASCADES project (https://c-cascades.ulb.ac.be/) funded by the European Union's Horizon 2020 research and innovation program under the Marie Sklodowska-Curie grant agreement No. 643052. We are grateful to Pierre Regnier for leading this effort. Financial support was provided by the Swiss Government (Staatsskretariat für Bildung, Forschung und Innovation—SBFI) and ETH Zürich. We would also like to thank Cara Nissen for her valuable insight on the BEC model and Damian Loher for technical support. Finally, we thank Victoria Coles and a second reviewer for their thoughtful and constructive reviews that helped to improve the paper.

References

Aller, R. C., Blair, N. E., Xia, Q., & Rude, P. D. (1996). Remineralization rates, recycling, and storage of carbon in Amazon shelf sediments. *Continental Shelf Research*, *16*(5–6), 753–786. https://doi.org/10.1016/0278-4343(95)00046-1

Anderson, L. A., & Sarmiento, J. L. (1994). Redfield ratios of remineralization determined by nutrient data analysis. *Global Biogeochemical Cycles*, *8*(1), 65–80. https://doi.org/10.1029/93GB03318

Araujo, M., Noriega, C., Hounsou-gbo, G. A., Veleda, D., Araujo, J., Bruto, L., et al. (2017). A synoptic assessment of the Amazon River-ocean continuum during boreal autumn: From physics to plankton communities and carbon flux. *Frontiers in Microbiology*, *8*(7), 1–18. https://doi.org/10.3389/fmicb.2017.01358

Araujo, M., Noriega, C., & LefÃ¨vre, N. (2014). Nutrients and carbon fluxes in the estuaries of major rivers flowing into the tropical Atlantic. *Frontiers Marine Science*, *1*. https://doi.org/10.3389/fmars.2014.00010

Armstrong, R. A., Lee, C., Hedges, J. I., Honjo, S., & Wakeham, S. G. (2001). A new, mechanistic model for organic carbon fluxes in the ocean based on the quantitative association of POC with ballast minerals. *Deep-Sea Research Part II Topical Studies in Oceanography*, *49*(1–3), 219–236. https://doi.org/10.1016/S0967-0645(01)00101-1

Berner, R. A., & Rao, J.-L. (1994). Phosphorus in sediments of the Amazon River and estuary: Implications for the global flux of phosphorus to the sea. *Geochimica et Cosmochimica Acta*, *58*(10), 2333–2339. https://doi.org/10.1016/0016-7037(94)90014-0

Beusen, A. (2014). *Transport of nutrients from land to sea: Global modeling approaches and uncertainty analyses (No. 58)*. Department of Earth Sciences, Utrech University.

Brzezinski, M. A., Dickson, M.-L., Nelson, D. M., & Sambrotto, R. (2003). Ratios of Si, C, and N uptake by microplankton in the Southern Ocean. *Deep Sea Research Part II: Topical Studies in Oceanography*, *50*(3–4), 619–633. https://doi.org/10.1016/S0967-0645(02)00587-8

Chien, C.-T., Mackey, K. R. M., Dutkiewicz, S., Mahowald, N. M., Prospero, J. M., & Paytan, A. (2016). Effects of African dust deposition on phytoplankton in the western tropical Atlantic Ocean off Barbados. *Global Biogeochemical Cycles*, *30*(5), 716–734. https://doi.org/10.1002/2015GB005334

Coles, V. J., Brooks, M. T., Hopkins, J., Stukel, M. R., Yager, P. L., & Hood, R. R. (2013). The pathways and properties of the Amazon River plume in the tropical North Atlantic Ocean. *Journal of Geophysics Research: Oceans*, *118*(12), 6894–6913. https://doi.org/10.1002/2013JC008981

Coles, V. J., & Hood, R. R. (2006). Modeling the impact of iron and phosphorus limitations on nitrogen fixation in the Atlantic Ocean. sep. *Biogeosciences Discussions*, *3*(5), 1391–1451. https://doi.org/10.5194/bgd-3-1391-2006

Cooley, S. R., Coles, V. J., Subramaniam, A., & Yager, P. L. (2007). Seasonal variations in the Amazon plume-related atmospheric carbon sink. *Global Biogeochemical Cycles*, *21*(3). https://doi.org/10.1029/2006GB002831

Da Cunha, L. C., & Buitenhuis, E. T. (2013). Riverine influence on the tropical Atlantic Ocean biogeochemistry. *Biogeosciences*, *10*(10), 6357–6373. https://doi.org/10.5194/bg-10-6357-2013

Dagg, M., Benner, R., Lohrenz, S., & Lawrence, D. (2004). Transformation of dissolved and particulate materials on continental shelves influenced by large rivers: Plume processes. *Continental Shelf Research*, *24*(7–8), 833–858. https://doi.org/10.1016/j.csr.2004.02.003

Dai, A., Qian, T., Trenberth, K. E., & Milliman, J. D. (2009). Changes in continental freshwater discharge from 1948 to 2004. *Journal of Climate*, *22*(10), 2773–2792. https://doi.org/10.1175/2008JCLI2592.1

Dee, D. P., Uppala, S. M., Simmons, A. J., Berrisford, P., Poli, P., Kobayashi, S., et al. (2011). The era-interim reanalysis: Configuration and performance of the data assimilation system. *Quarterly Journal of the Royal Meteorological Society*, *137*(656), 553–597. https://doi.org/10.1002/qj.828

Del Vecchio, R., & Subramaniam, A. (2004). Influence of the Amazon River on the surface optical properties of the western tropical North Atlantic Ocean. *Journal of Geophysical Research*, *109*. https://doi.org/10.1029/2004JC002503

DeMaster, D., McKee, B., Moore, W., Nelson, D., Showers, W., & Smith, W. (1991). Geochemical processes occurring in the waters at the Amazon River/Ocean boundary. *Oceanog*, *4*(1), 15–20. https://doi.org/10.5670/oceanog.1991.16

Demaster, D. J., & Aller, R. C. (2001). *The biogeochemistry of the amazon basin*. New York, NY: Oxford University Press. .

Demaster, D. J., & Pope, R. H. (1996). Nutrient dynamics in Amazon shelf waters: Results from AMASSEDS. *Continental Shelf Research*, *16*(3), 263–289. https://doi.org/10.1016/0278-4343(95)00008-O

Dickson, A. G., Sabine, C. L., & Christian, J. R. (2007). *Guide to Best Practices for Ocean CO_2 Measurements. PICES Special Publication* (Vol. 3).

Doherty, M., Yager, P. L., Moran, M. A., Coles, V. J., Fortunato, C. S., Krusche, A. V., et al. (2017). Bacterial biogeography across the Amazon River-ocean continuum. *Frontiers in Microbiology*, *8*(5), 1–17. https://doi.org/10.3389/fmicb.2017.00882

Dunne, J. P., Sarmiento, J. L., & Gnanadesikan, A. (2007). A synthesis of global particle export from the surface ocean and cycling through the ocean interior and on the seafloor. *Global Biogeochemical Cycles*, *21*(4). https://doi.org/10.1029/2006GB002907

Fontes, R. F. C., Castro, B. M., & Beardsley, R. C. (2008). Numerical study of circulation on the inner Amazon Shelf. *Ocean Dynamics*, *58*(3–4), 187–198. https://doi.org/10.1007/s10236-008-0139-4

Foster, R. A., Kuypers, M. M. M., Vagner, T., Paerl, R. W., Musat, N., & Zehr, J. P. (2011). Nitrogen fixation and transfer in open ocean diatom-cyanobacterial symbioses. *The ISME Journal*, *5*(9), 1484–1493. https://doi.org/10.1038/ismej.2011.26

Foster, R. A., & O'Mullan, G. D. (2008). Nitrogen-Fixing and Nitrifying Symbioses in the Marine Environment. *Nitrogen in the Marine Environment*, 1197–1218. https://doi.org/10.1016/B978-0-12-372522-6.00027-X

Foster, R. A., Subramaniam, A., Mahaffey, C., Carpenter, E. J., Capone, D. G., & Zehr, J. P. (2012). Influence of the Amazon River plume on distributions of free-living and symbiotic cyanobacteria in the western tropical north Atlantic Ocean. *Limnology & Oceanography*, *52*(2), 517–532. https://doi.org/10.4319/lo.2007.52.2.0517

Frischknecht, M., Münnich, M., & Gruber, N. (2018). Origin, transformation, and fate: The three-dimensional biological pump in the California current system. *Journal of Geophysics Research: Oceans*, *123*(11), 7939–7962. https://doi.org/10.1029/2018JC013934

Garcia, H. E., Locarnini, R., Boyer, T. P., Antonov, J. I., Baranova, O. K., Zweng, M. M., & Johnson, D. R. (2013). World Ocean Atlas 2013 Volume 4: Nutrients phosphate, nitrate, silicate). *NOAA Atlas NESDIS 76*, *4*(9), 396. .

Girault, M., Arakawa, H., & Hashihama, F. (2013). Phosphorus stress of microphytoplankton community in the western subtropical North Pacific. *Journal of Plankton Research*, *35*(1), 146–157. https://doi.org/10.1093/plankt/fbs076

GLOBALVIEW-CO2. (2014). *Coperative Atmospheric Data IntegrationProject – Carbon Dioxide, CD-ROM, NOAA ESRL*, Boulder, Colorado. Also available on Internet via anonymous FTP toftp.cmdl.noaa.gov.

Goes, J. I., Gomes, H. D. R., Chekalyuk, A. M., Carpenter, E. J., Montoya, J. P., Coles, V. J., et al. (2014). Influence of the Amazon River discharge on the biogeography of phytoplankton communities in the western tropical north Atlantic. *Progress in Oceanography*, *120*, 29–40. https://doi.org/10.1016/j.pocean.2013.07.010

Gouveia, N. A., Gherardi, D. F. M., Wagner, F. H., Paes, E. T., Coles, V. J., & Aragão, L. E. O. C. (2019). The salinity structure of the Amazon River plume drives spatiotemporal variation of oceanic primary productivity. *Journal of Geophysics Research: Biogeoscience*, *124*(1), 147–165. https://doi.org/10.1029/2018JG004665

Goyet, C., Adams, R., & Eischeid, G. (1998). Observations of the CO_2 system properties in the tropical Atlantic Ocean. *Marine Chemistry*, *60*(1), 49–61. https://doi.org/10.1016/S0304-4203(97)00081-9

Hansell, D. A., & Follows, M. J. (2008). *Nitrogen in the Atlantic Ocean*. Elsevier Inc. https://doi.org/10.1016/B978-0-12-372522-6.00013-X

Ibánhez, J. S. P., Flores, M., & Lefèvre, N. (2017). Collapse of the tropical and subtropical North Atlantic CO_2 sink in boreal spring of 2010. *Scientific Reports*, *7*, 1–9. https://doi.org/10.1038/srep41694

Jin, X., Gruber, N., Frenzel, H., Doney, S. C., & McWilliams, J. C. (2008). The impact on atmospheric CO_2 of iron fertilization induced changes in the ocean's biological pump. *Biogeosciences*, *5*(2), 385–406. https://doi.org/10.5194/bg-5-385-2008

Kalnay, E., Kanamitsu, M., Kistler, R., Collins, W., Deaven, D., Gandin, L., et al. (1996). The NCEP/NCAR 40-year reanalysis project. *Bulletin of the American Meteorological Society*, *77*(3), 437–471. https://doi.org/10.1175/1520-0477(1996)077<0437:TNYRP>2.0.CO;2

Korte, L. F., Brummer, G. J. A., Does, M., Guerreiro, C. V., Mienis, F., Munday, C. I., et al. (2020). Multiple drivers of production and particle export in the western tropical North Atlantic. *Limnology & Oceanography*, *65*, 2108–2124. https://doi.org/10.1002/lno.11442

Körtzinger, A. (2003). A significant CO_2 sink in the tropical Atlantic Ocean associated with the Amazon River plume. *Geophysical Research Letters*, *30*(24), 2–5. https://doi.org/10.1029/2003GL018841

Lacroix, F., Ilyina, T., & Hartmann, J. (2020). Oceanic CO_2 outgassing and biological production hotspots induced by pre-industrial river loads of nutrients and carbon in a global modeling approach. *Biogeosciences*, *17*(1), 55–88. https://doi.org/10.5194/bg-17-55-2020

Landschützer, P., Gruber, N., Bakker, D. C. E., & Schuster, U. (2014). Recent variability of the global ocean carbon sink. *Global Biogeochemical Cycles*, *28*(9), 927–949. https://doi.org/10.1002/2014GB004853

Langlois, R. J., Hümmer, D., & LaRoche, J. (2008). Abundances and distributions of the dominant nifH phylotypes in the Northern Atlantic Ocean. *Aemilianense*, *74*(6), 1922–1931. https://doi.org/10.1128/AEM.01720-07

Laufkötter, C., Vogt, M., Gruber, N., Aumont, O., Bopp, L., Doney, S. C., et al. (2016). Projected decreases in future marine export production: The role of the carbon flux through the upper ocean ecosystem. *Biogeosciences*, *13*(13), 4023–4047. https://doi.org/10.5194/bg-13-4023-2016

Lauvset, S. K., Key, R. M., Olsen, A., Van Heuven, S., Velo, A., Lin, X., et al. (2016). A new global interior ocean mapped climatology: The 1° × 1° GLODAP version 2. *Earth System Science Data*, *8*(2), 325–340. https://doi.org/10.5194/essd-8-325-2016

Lefévre, N., Diverrés, D., & Gallois, F. (2010). Origin of CO_2 undersaturation in the western tropical Atlantic. *Tellus B: Chemical and Physical Meteorology*, *62*(5), 595–607. https://doi.org/10.1111/j.1600-0889.2010.00475.x

Lefèvre, N., Flores Montes, M., Gaspar, F. L., Rocha, C., Jiang, S., De Araújo, M. C., & Ibánhez, J. S. P. (2017). Net Heterotrophy in the Amazon Continental Shelf Changes Rapidly to a Sink of CO_2 in the Outer Amazon Plume. *Frontiers Marine Science*, *4*, 1–16. https://doi.org/10.3389/fmars.2017.00278

Lefèvre, N., Moore, G., Aiken, J., Watson, A., Cooper, D., & Ling, R. (1998). Variability of pCO_2 in the tropical Atlantic in 1995. *Journal of Geophysical Research*, *103*, 5623–5634. https://doi.org/10.1029/97jc02303

Lefèvre, N., Urbano, D. F., Gallois, F., & Diverres, D. (2014). Impact of physical processes on the seasonal distribution of the fugacity of CO_2 in the western tropical Atlantic. *Journal of Geophysical Research: Oceans*, 1–18. https://doi.org/10.1002/2013JC009248.Received

Letelier, R., & Karl, D. (1998). Trichodesmium spp. physiology and nutrient fluxes in the north pacific subtropical gyre. *Aquatic Microbial Ecology*, *15*(3), 265–276. https://doi.org/10.3354/ame015265

Levitus, S., Boyer, T. P., Garcia, H. E., Locarnini, R. A., Zweng, M. M., Mishonov, A. V., & Seidov, D. (2015). *World Ocean Atlas 2013 (NCEI Accession 0114815)*. NOAA National Centers for Environmental Information. *Dataset*. https://doi.org/10.7289/v5f769gt

Lovecchio, E., Gruber, N., Münnich, M., & Lachkar, Z. (2017). On the long-range offshore transport of organic carbon from the Canary Upwelling System to the open North Atlantic. *Biogeosciences*, *14*(13), 3337–3369. https://doi.org/10.5194/bg-14-3337-2017

Lumpkin, R., & Garzoli, S. L. (2005). Near-surface circulation in the Tropical Atlantic Ocean. *Deep Sea Research Part I: Oceanographic Research Papers*, *52*(3), 495–518. https://doi.org/10.1016/j.dsr.2004.09.001

Lumpkin, R., & Johnson, G. C. (2013). Global ocean surface velocities from drifters: Mean, variance, El Niño-Southern Oscillation response, and seasonal cycle. *Journal of Geophysics Research: Oceans*, *118*(6), 2992–3006. https://doi.org/10.1002/jgrc.20210

Luo, Y.-W., Doney, S. C., Anderson, L. A., Benavides, M., Berman-Frank, I., Bode, A., et al. (2012). Database of diazotrophs in global ocean: Abundance, biomass and nitrogen fixation rates. *Earth System Science Data*, *4*(1), 47–73. https://doi.org/10.5194/essd-4-47-2012

Mahowald, N. M., Engelstaedter, S., Luo, C., Sealy, A., Artaxo, P., Benitez-Nelson, C., et al. (2009). Atmospheric Iron Deposition: Global Distribution, Variability, and Human Perturbations. *Annual Review Marine Science*, *1*(1), 245–278. https://doi.org/10.1146/annurev.marine.010908.163727

Medeiros, P. M., Seidel, M., Ward, N. D., Carpenter, E. J., Gomes, H. R., Niggemann, J., et al. (2015). Fate of the Amazon River dissolved organic matter in the tropical Atlantic Ocean. *Global Biogeochemical Cycles*, *29*, 677–690. https://doi.org/10.1002/2015GB005115.Received

Moore, J. K., Lindsay, K., Doney, S. C., Long, M. C., & Misumi, K. (2013). Marine ecosystem dynamics and biogeochemical cycling in the community earth system model [CESM1(BGC)]: Comparison of the 1990s with the 2090s under the RCP4.5 and RCP8.5 scenarios. *Journal of Climate*, *26*, 9291–9312. https://doi.org/10.1175/JCLI-D-12-00566.1

Pailler, K., Bourlès, B., & Gouriou, Y. (1999). The barrier layer in the western tropical Atlantic Ocean. *Geophysical Research Letters*, *26*(14), 2069–2072. https://doi.org/10.1029/1999GL900492

Richey, J. E., Victoria, R. L., Salati, E., & Forsberg, B. R. (1991). *Biogeochemistry of major world rivers*. New York, NY: John Wiley and Sons.

Sarmiento, J. L., & Gruber, N. (2006). *Ocean biogeochemical dynamics*. Princeton, NJ: Princeton University Press.

Schuster, U., McKinley, G. a., Bates, N., Chevallier, F., Doney, S. C., Fay, a. R., et al. (2013). An assessment of the Atlantic and Arctic sea-air CO2 fluxes, 1990-2009. *Biogeosciences*, *10*(1), 607–627. https://doi.org/10.5194/bg-10-607-2013

Seitzinger, S. P., Harrison, J. A., Dumont, E., Beusen, A. H. W., & Bouwman, A. F. (2005). Sources and delivery of carbon, nitrogen, and phosphorus to the coastal zone: An overview of Global Nutrient Export from Watersheds (NEWS) models and their application. *Global Biogeochemical Cycles*, *19*(4). https://doi.org/10.1029/2005GB002606

Shchepetkin, A. F., & McWilliams, J. C. (2005). The regional oceanic modeling system (ROMS): A split-explicit, free-surface, topography-following-coordinate oceanic model. *Ocean Modelling*, *9*(4), 347–404. https://doi.org/10.1016/j.ocemod.2004.08.002

Shu, C.-W. (1998). Essentially non-oscillatory and weighted essentially non-oscillatory schemes for hyperbolic conservation laws. In A. Quarteroni (Ed.), *Advanced numerical approximation of nonlinear hyperbolic equations: Lectures given at the 2nd session of the centro internazionale matematico estivo (c.i.m.e.) held in cetraro, Italy* (pp. 325–432). Berlin,: Springer Berlin Heidelberg. https://doi.org/10.1007/BFb0096355

Smith, W. O., & Demaster, D. J. (1996). Phytoplankton biomass and productivity in the Amazon River plume: Correlation with seasonal river discharge. *Continental Shelf Research*, *16*(3), 291–319. https://doi.org/10.1016/0278-4343(95)00007-N

Soetaert, K., Herman, P. M. J., & Middelburg, J. J. (1996). A model of early diagenetic processes from the shelf to abyssal depths. *Geochimica et Cosmochimica Acta*, *60*(6), 1019–1040. https://doi.org/10.1016/0016-7037(96)00013-0

Sohm, J. A., & Capone, D. G. (2010). Zonal differences in phosphorus pools, turnover and deficiency across the tropical North Atlantic Ocean. *Global Biogeochemical Cycles*, *24*(2). https://doi.org/10.1029/2008GB003414

Stramma, L., & Schott, F. (1999). The mean flow field of the tropical Atlantic Ocean. *Deep Sea Research Part II: Topical Studies in Oceanography*, *46*(1–2), 279–303. https://doi.org/10.1016/S0967-0645(98)00109-X

Stukel, M. R., Coles, V. J., Brooks, M. T., & Hood, R. R. (2014). Top-down, bottom-up and physical controls on diatom-diazotroph assemblage growth in the Amazon River plume. *Biogeosciences*, *11*(12), 3259–3278. https://doi.org/10.5194/bg-11-3259-2014

Subramaniam, A., Yager, P. L., Carpenter, E. J., Mahaffey, C., Björkman, K., Cooley, S., et al. (2008). Amazon River enhances diazotrophy and carbon sequestration in the tropical north Atlantic Ocean. *Proceedings of the National Academy of Sciences*, *105*(30), 10460–10465. https://doi.org/10.1073/pnas.0710279105

Takahashi, T., Sutherland, S. C., Wanninkhof, R., Sweeney, C., Feely, R. A., Chipman, D. W., et al. (2009). Climatological mean and decadal change in surface ocean pCO_2, and net sea-air CO_2 flux over the global oceans. *Deep Sea Research Part II: Topical Studies in Oceanography*, *56*(8), 554–577. https://doi.org/10.1016/j.dsr2.2008.12.009

Ternon, J. F., Oudot, C., Dessier, A., & Diverres, D. (2000). A seasonal tropical sink for atmospheric CO_2 in the Atlantic Ocean: The role of the Amazon River discharge. *Marine Chemistry*, *68*(3), 183–201. https://doi.org/10.1016/S0304-4203(99)00077-8

Torres-Valdés, S., Tsubouchi, T., Bacon, S., Naveira-Garabato, A. C., Sanders, R., McLaughlin, F. A., et al. (2013). Export of nutrients from the Arctic Ocean. *Journal of Geophysics Research: Oceans*, *118*(4), 1625–1644. https://doi.org/10.1002/jgrc.20063

Tyler, A. N., Hunter, P. D., Spyrakos, E., Groom, S., Constantinescu, A. M., & Kitchen, J. (2016). Developments in earth observation for the assessment and monitoring of inland, transitional, coastal and shelf-sea waters. *The Science of the Total Environment*, *572*, 1307–1321. https://doi.org/10.1016/j.scitotenv.2016.01.020

Vandemeulebrouck, R. (2020). *Implementation and analysis of a weno scheme (Unpublished master's thesis)*. Faculty of Maths, Computational Science - CSE EPFL.

Wang, W.-L., Moore, J. K., Martiny, A. C., & Primeau, F. W. (2019). Convergent estimates of marine nitrogen fixation. *Nature*, *566*(7743), 205–211. https://doi.org/10.1038/s41586-019-0911-2

Ward, N. D., Bianchi, T. S., Medeiros, P. M., Seidel, M., Richey, J. E., Keil, R. G., & Sawakuchi, H. O. (2017). Where carbon goes when water flows: carbon cycling across the aquatic continuum. *Frontiers Marine Science*, *4*. https://doi.org/10.3389/fmars.2017.00007

Watkins-Brandt, K., Letelier, R., Spitz, Y., Church, M., Böttjer, D., & White, A. (2011). Addition of inorganic or organic phosphorus enhances nitrogen and carbon fixation in the -oligotrophic North Pacific. *Marine Ecology Progress Series*, *432*, 17–29. https://doi.org/10.3354/meps09147

Weber, S. C., Carpenter, E. J., Coles, V. J., Yager, P. L., Goes, J., & Montoya, J. P. (2017). Amazon River influence on nitrogen fixation and export production in the western tropical North Atlantic. *Limnology & Oceanography*, *62*(2), 618–631. https://doi.org/10.1002/lno.10448

Westberry, T., Behrenfeld, M. J., Siegel, D. A., & Boss, E. (2008). Carbon-based primary productivity modeling with vertically resolved photoacclimation. *Global Biogeochemical Cycles*, *22*(2). https://doi.org/10.1029/2007GB003078

Yang, S., Gruber, N., Long, M. C., & Vogt, M. (2017). ENSO-driven variability of denitrification and suboxia in the eastern tropical Pacific Ocean. *Global Biogeochemical Cycles*, *31*(10), 1470–1487. https://doi.org/10.1002/2016GB005596

Yeung, L. Y., Berelson, W. M., Young, E. D., Prokopenko, M. G., Rollins, N., Coles, V. J., et al. (2012). Impact of diatom-diazotroph associations on carbon export in the Amazon River plume. *Geophysical Research Letters*, *39*(17), 1–6. https://doi.org/10.1029/2012GL053356